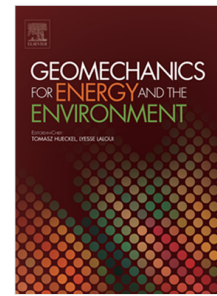


## Journal Pre-proof

Experimental analysis of a thermoactive underground railway station

Jacopo Zannin, Alessio Ferrari, Tohid Kazerani, Azad Koliji,  
Lyesse Laloui



PII: S2352-3808(21)00043-5  
DOI: <https://doi.org/10.1016/j.gete.2021.100275>  
Reference: GETE 100275

To appear in: *Geomechanics for Energy and the Environment*

Received date: 27 May 2021  
Revised date: 1 September 2021  
Accepted date: 4 October 2021

Please cite this article as: J. Zannin, A. Ferrari, T. Kazerani et al., Experimental analysis of a thermoactive underground railway station, *Geomechanics for Energy and the Environment* (2021), doi: <https://doi.org/10.1016/j.gete.2021.100275>.

This is a PDF file of an article that has undergone enhancements after acceptance, such as the addition of a cover page and metadata, and formatting for readability, but it is not yet the definitive version of record. This version will undergo additional copyediting, typesetting and review before it is published in its final form, but we are providing this version to give early visibility of the article. Please note that, during the production process, errors may be discovered which could affect the content, and all legal disclaimers that apply to the journal pertain.

© 2021 The Author(s). Published by Elsevier Ltd. This is an open access article under the CC BY-NC-ND license (<http://creativecommons.org/licenses/by-nc-nd/4.0/>).

## 1 Experimental analysis of a thermoactive underground railway station

2 Jacopo Zannin<sup>(\*,1)</sup>, Alessio Ferrari<sup>(1,2)</sup>, Tohid Kazerani<sup>(3)</sup>, Azad Koliji<sup>(3)</sup>, Lyesse Laloui<sup>(1)</sup>

3 <sup>(1)</sup> Swiss Federal Institute of Technology in Lausanne, EPFL, Laboratory of Soil Mechanics, EPFL-  
4 ENAC-IIC-LMS, Station 18, 1015 Lausanne, Switzerland

5 <sup>(2)</sup> Università degli Studi di Palermo, Engineering Department, Italy

6 <sup>(3)</sup> BG Consulting Engineers, Av. de Cour 61, 1007 Lausanne

7 \* Corresponding author e-mail: jacopo.zannin@gmail.com

### 8 9 Abstract

10 Little is known about the real energy potential of thermoactive underground infrastructures, such as  
11 railway stations, that can act as a heating/cooling provider for the built environment. This study presents  
12 the results of thermomechanical full-scale in situ testing and numerical analysis of a thermoactive  
13 underground train station. The thermal performance and related geostructural impact of a portion of the  
14 new underground energy infrastructure (UEI) installed at the Lancy-Bachet train station in Geneva  
15 (Switzerland) are analyzed. Heating and cooling tests simulating real operative geothermal conditions  
16 are considered. Particular attention is given to (i) the monitored wall-tunnel hydrothermal interactions,  
17 (ii) the thermal response of the UEI to heating/cooling thermal inputs and (iii) the thermomechanical  
18 behavior of the energy geostructure. Among the main results of this study, it is shown how the  
19 hydrothermal tunnel behavior considerably varies on a seasonal basis, while the train circulation  
20 completely drives the airflow in the tunnel. The UEI shows a strong heat storage potential due to the  
21 main conductive heat transfers between the geostructure and soil, while lower heat fluxes are detected  
22 at the wall-tunnel interface. The extraction potential is of lower magnitude **with respect to storage**  
23 because of the limited range of operative fluid temperatures and of the concurrent action of temperature  
24 variations at the tunnel boundaries affecting the materials within the UEI. Preliminary guidelines for  
25 the thermal response test execution on underground thermoactive infrastructures are also reported. The  
26 monitored thermomechanical behavior suggests different wall behaviors in the vertical and longitudinal  
27 directions. Low-magnitude strains are recorded, while the mechanical capacity of the existing  
28 geostructure can satisfactorily sustain concurrent thermomechanical actions.

### 29 30 Keywords

31 Energy geostructures; Energy walls; Underground infrastructures; Thermomechanical behavior; Soil-  
32 structure interaction; Thermal response test

## 33 1. Introduction

34 Thermal activation of shallow underground infrastructures may represent an important source of  
35 thermal energy for the built environment. In recent years, an increasing number of installations using  
36 shallow geothermal technologies (e.g., energy geostructures, EGs) have been recorded around the world  
37 (Laloui & Rotta Loria, 2019). In EGs, the dual role of geostructures is enhanced: they involve structural  
38 support and a geothermal heat exchanger role. The EG has proven to be an efficient renewable solution  
39 for heating/cooling of the built environment (Sutman et al., 2020). This technology has been approached  
40 by the scientific community and shows a promising future (Brandl, 2006; Laloui and Rotta Loria, 2019).  
41 Examples of underground energy infrastructures (UEIs) include but are not limited to underground  
42 circular and cut-and-cover tunnels used for transportation and/or services, underground train stations,  
43 trenches, and sewers. Within UEIs, heat exchangers (i.e., plastic pipes) can be secured to the steel cage  
44 of the reinforced concrete geostructure, and they exchange heat with the surrounding materials by  
45 circulating a fluid.

46 Knowledge on UEIs lacks feedback from real monitored installations, whose experience could be  
47 crucial to fully understand the performance of ongoing multiphysical processes and to allow design  
48 optimization strategies and guidelines for future installations. In this regard, few field experiments are  
49 available in the literature. Attempts to understand the thermal behavior highlighted that the heat  
50 exchanger (HE) configuration plays a crucial role and that wall-tunnel thermal interactions could be  
51 non-negligible (Xia et al., 2012; Nicholson et al. 2014). Different thermal performances for energy  
52 walls (EWs) and slabs were recorded, with the former outperforming the latter for the particular case  
53 study presented in Sterpi et al. (2018, 2020). As regard to the thermomechanical behavior, low-  
54 magnitude thermally induced deformations were registered at the Lainzer U2 line in Vienna (Brandl,  
55 2016). The complex multiphysical aspects involved within UEI operations make it difficult to  
56 thoroughly understand and describe their thermal, hydraulic and mechanical behavior (Loveridge et al.,  
57 2020). From an energy performance perspective, the thermal response test (i.e., TRT) execution for UEI  
58 is challenging, as reported by Makasis et al. (2020) and Shafagh et al. (2020). Despite the interesting  
59 knowledge acquired from these studies, no guidelines for TRT execution on geostructures facing air  
60 interfaces are available.

61 Exploiting a new UEI installation in Geneva (Switzerland), thermo-hydro-mechanical (THM) in situ  
62 tests were possible. This represented a unique opportunity to further investigate fundamental aspects  
63 linked to the multiphysical behavior of UEIs, as well as to develop preliminary guidelines for successful  
64 THM in situ test execution. The UEI was tested under real operational conditions, which means that it  
65 was subjected to heating/cooling geothermal operations along with mechanical and environmental  
66 actions. The study was conducted with the following objectives: (i) to investigate the real THM behavior  
67 of the UEI through a series of full-scale in situ experimental tests upon heating and cooling thermal  
68 inputs; (ii) to understand the rationale behind fundamental THM aspects linked to thermal activation of  
69 underground infrastructures; and (iii) to propose preliminary guidelines for in situ test execution.

70 In this paper, after a description of the tested site and experimental setup, hydrothermal aspects are  
71 approached, followed by thermomechanical ones. Experimental results are presented, discussed and  
72 interpreted with the help of numerical simulations validated against experimental results, which allow  
73 us to have a complete picture of the THM aspects involved in UEI operation. Concluding remarks on  
74 the geothermal exploitation of the tested UEI are finally reported.

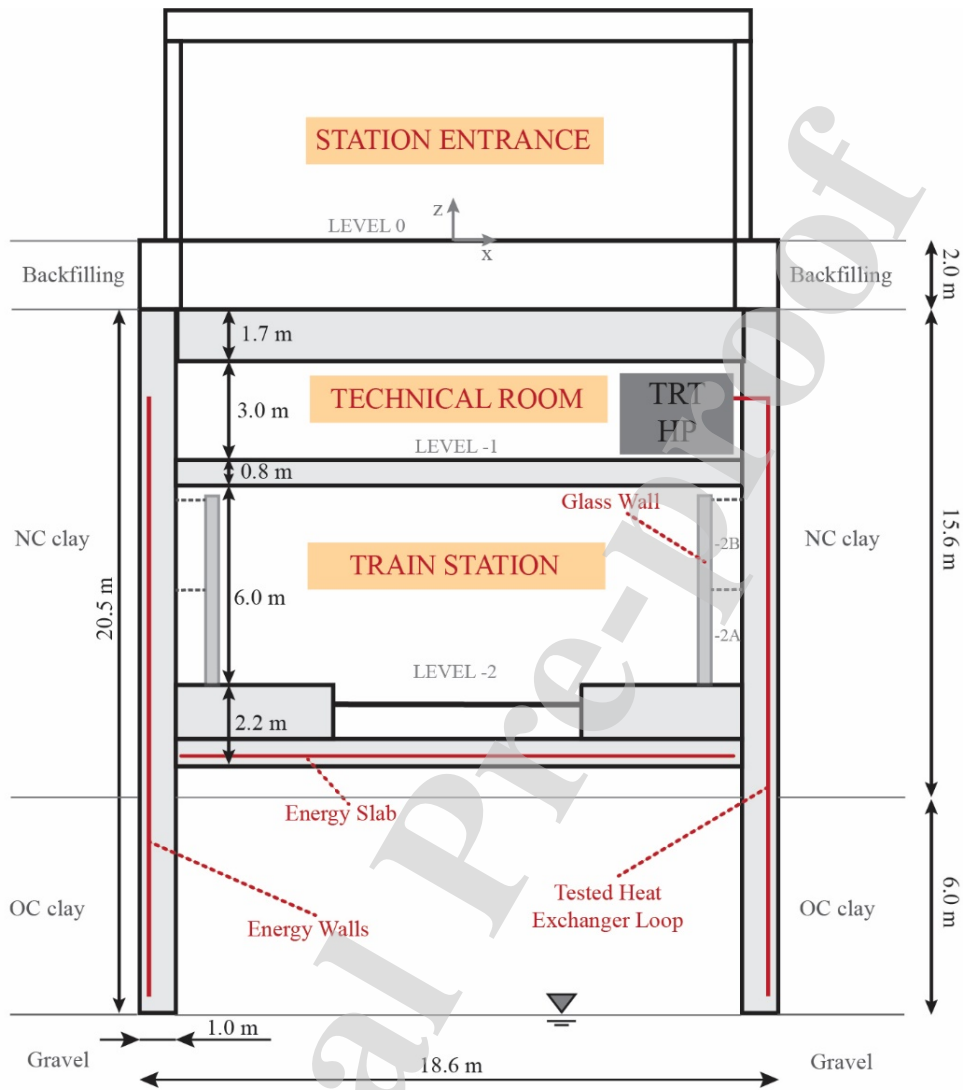
## 75 2. The experimental campaign

76 In this section, the implemented energy geostructure is outlined, and then the experimental campaign  
77 and setup is described.

### 78 2.1. The tested energy geostructure

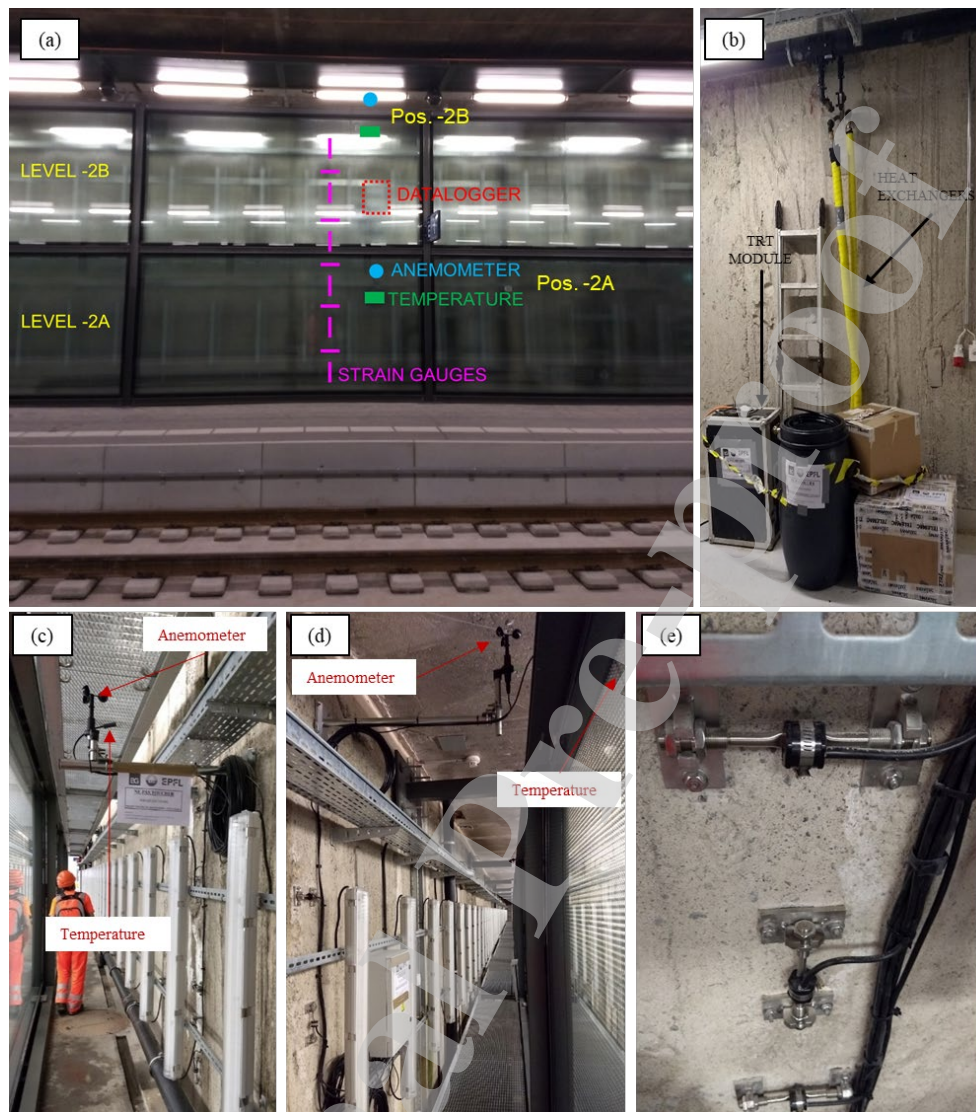
79 The tested site is located in the southwestern part of Geneva, Switzerland. A new railway line that  
80 connects Geneva to Annemasse (France) was recently constructed. One of the train stations, Lancy-  
81 Bachet, is equipped with EWs and energy slabs presenting a total thermoactive surface of approximately  
82 5000 m<sup>2</sup>. In plain view, the train station represents the entrance point of the underground tunnel portion,  
83 going toward Annemasse. A vertical cross section is depicted in Figure 1, while photos of the site are  
84 shown in Figure 2. The accessible underground space consists of two levels (Figure 1), where the  
85 bottom level (level -2) is the railway level. At level -2, an architectural element composed of a glass  
86 wall sustained by a steel structure is installed at a distance of 1 m from the concrete walls (Figure 1 and  
87 Figure 2(a)). The space between these two walls is partly separated into two regions by a steel grid,  
88 hereafter named levels -2A and -2B (Figure 1 and Figure 2(a), respectively). This architectural choice  
89 will affect the airflow near the wall, a topic that will be further expanded later in this paper. A technical  
90 room is located at level -1. The train station entrance for the passengers is at the ground level (level 0).

91



93 Figure 1 Cross section of the Lancy-Bachet underground train station with an indication of the heat exchanger locations

94



96 Figure 2 (a) Global view of level -2 with an indication of the monitoring system; (b) details of level -1 with a description of  
 97 the equipment used to perform the geothermal tests; (c) temperature sensor and anemometer at level -2A; (d) temperature  
 98 sensor and anemometer at level -2B; and (e) partial view of the strain gauges

99 The vertical walls surrounding the train station and the base slab are equipped with HEs. The vertical  
 100 walls are equipped with one U-loop every 2.5 m in the tunnel longitudinal direction, with a pipe spacing  
 101 of 0.25 m and external and inner pipe diameters of 25 mm and 23 mm, respectively. The total length  
 102 of each heat exchanger circuit in the walls is 36 m. The HEs are installed inside the concrete  
 103 geostructure, attached to the reinforcement cage and placed at a distance 0.20 m from the wall-soil  
 104 interface. The walls are 1 m thick, which means that the HEs are placed at a distance 0.80 m from the  
 105 wall-air interface facing the tunnel. The 2.2 m thick slab is equipped with heat exchanger loops having  
 106 a slinky shape and pipe spacing of 0.5 m. Every heat exchanger circuit in the wall and slab is connected  
 107 in parallel to the main pipe connections. The entire piping system is eventually collected in a technical

108 room. The portion tested in this study is composed of one single heat exchanger U-loop of the wall. **The**  
 109 **authors were not allowed to test larger portions of the UEI because of access restrictions.**

110 The soil profile (Figure 1) is characterized by a backfilling layer in the first 2.0 m, a layer of normally  
 111 consolidated (NC) clay until a depth  $z = -17.6$  m, a layer of slightly overconsolidated clay (OC) until  
 112  $z = -23.6$  m, and a layer of dense gravel at the bottom, which hosts the groundwater table. During soil  
 113 characterization, all soil layers were fully saturated, as from the analyses on samples taken from the  
 114 site. Table 1 reports the material properties, where  $E$  is the Young modulus,  $\nu$  is the Poisson ratio,  $\gamma_{sat}$   
 115 is the unit weight for saturated conditions,  $n$  is the porosity, and  $\alpha$  is the thermal expansion coefficient.  
 116 The material properties for the NC clay and OC clay are determined on the basis of an analysis of  
 117 samples taken from the site. The material properties of the backfilling and gravel materials were  
 118 determined on the basis of a literature review (Bowles, 1988; Lambe and Whitman, 1991). Thermal  
 119 properties are estimated through a dedicated in situ test (i.e., the TRT), as described in the following  
 120 section 4.2.

121

Table 1 Material properties

Material	Thickness (m)	$E$ (MPa)	$\nu$ (-)	$\gamma_{sat}$ (kN/m <sup>3</sup> )	$n$ (-)	$\alpha_{th}$ (K <sup>-1</sup> )
Backfill	1.92	30	0.30	19.6	0.35	$10^{-5}$
NC clay	15.60	19.9	0.30	19.7	0.35	$10^{-5}$
OC clay	5.98	41.6	0.30	20.2	0.37	$10^{-5}$
Gravel	37.91	150	0.25	22.5	0.21	$10^{-5}$
Reinforced Concrete	Structural geometry	28000	0.25	26.7	0.10	$10^{-5}$

122

## 123 2.2. The testing campaign

124 The testing campaign contained two phases. First, a TRT was executed in August 2019, following the  
 125 available standards (GSHPA, 2012). Second, heat pump (HP) tests were performed, which allowed us  
 126 to execute heating and cooling tests at constant inflow temperature and simulate real geothermal  
 127 operation scenarios. HP tests were executed in December 2019 (heating) and March 2020 (cooling). To  
 128 execute and monitor the experimental tests under different geothermal operation modes, a dedicated  
 129 monitoring system was designed by the authors to monitor the hydrothermal behavior of the heat carrier  
 130 fluid (HCF) inside the heat exchangers and the hydrothermal behavior of the air environment at levels  
 131 -1 and -2 and to record wall intrados deformations at level -2 (Figure 1 and Figure 2). The experimental  
 132 equipment used during the tests is installed at two levels (-1 and -2), which are separated and do not  
 133 communicate with one another.

134 The equipment installed at level -1 is, in the first stage, the heating module, called the TRT module  
135 (Mattsson et al., 2008), which is connected to the HE circuit Figure 2(b). The TRT module applies  
136 constant thermal power to the HE circuit, as is usually employed for standard TRTs (Gehlin &  
137 Hellström, 2000; Gehlin, 2002; Laloui et al., 2006; Mattsson et al., 2008; Sanner et al., 2005). In a later  
138 stage, the TRT module was replaced by a water-to-air HP (i.e., a commercial heat pump: Ciat Ereba  
139 11HT He), which allows heating/cooling tests to be performed by imposing the temperature at the  
140 inflow point of the HE circuit (i.e., the HP outflow). For the TRT module and the HP, a dedicated  
141 hydrothermal monitoring system is installed, allowing continuous (i.e., one record every 30 seconds)  
142 monitoring of the following parameters: (i) the HCF temperature at the inflow and return end of the HE  
143 circuit, (ii) the HCF flow rate, and (iii) the air temperature at the HP ventilator, inside the TRT module  
144 and of the undisturbed air of level -1.

145 The equipment installed at level -2 consists of a thermomechanical monitoring system (Figure 2 (a))  
146 specifically designed for this tested site (Zannin, 2020). The monitoring system is designed to allow the  
147 measurement of key parameters that govern the heat fluxes and the hydrothermal heat exchanges  
148 between the EG and tunnel air, as well as the wall intrados deformations. It allows real-time monitoring  
149 (i.e., one record every 5 minutes) of (i) air temperature and (ii) the wind speed in the tunnel and (iii)  
150 structural deformations at the wall intrados. Air temperature and velocity are measured through  
151 temperature sensors and anemometers (i.e., a resolution of  $0.1^{\circ}\text{C}$  for temperature and  $0.05\text{ m/s}$  for wind  
152 velocity) placed at two locations (pos. -2A and pos. -2B in Figure 2(a,c,d)): at the top part in front of  
153 the glass wall (i.e., Pos. -2B) to monitor the train station environment; in the bottom part behind the  
154 glass wall (i.e., Pos. -2A) to monitor the environment behind the glass wall. Structural monitoring is  
155 performed by employing deformation sensors (i.e., 11 uniaxial, vibrating wire strain gauges that read  
156 strain and temperature with a resolution of  $1\ \mu\epsilon$  and  $0.1^{\circ}\text{C}$ , respectively) that are screwed to the wall  
157 intrados and installed, alternatively, in the vertical and longitudinal directions (Figure 2(e)). The air  
158 temperature distribution near the wall intrados is captured through strain gauge readings. All the  
159 instruments are connected to a datalogger installed at level -2B. Because the geostructure was already  
160 partly constructed at the time of these experiments and the ground surface was a construction site, there  
161 was no possibility to install any monitoring system in the soil or inside the concrete geostructure. The  
162 data collected through this monitoring system enable a detailed assessment of the hydrothermal  
163 behavior of the train station environment (i.e., a time series of air temperature and wind speed) from  
164 August 2019 until June 2020. These experimental data allow for a detailed assessment of the boundary  
165 conditions of the numerical model reported in this work.

166 The experimental tests involving thermal activation of the HE circuit were of different types. First, a  
167 TRT was executed in August 2019. This test contained two phases: An initial phase of fluid circulation  
168 lasted 2 days, followed by the heating phase at a constant thermal power  $Q_{th} = 1\text{ kW} = 45\text{ W/m}$  of  
169 wall depth for 24 days. Second, the heat pump tests involved HCF heating (i.e., imposed inflow  
170 temperature  $T_{f,in} = 50.0^{\circ}\text{C}$ ) and cooling (i.e.,  $T_{f,in} = 1.0^{\circ}\text{C}$ ) tests and were performed between  
171 December 2019 and March 2020. Each test lasted approximately 2 weeks.



172

### 173 3. Hydrothermal behavior: experimental results

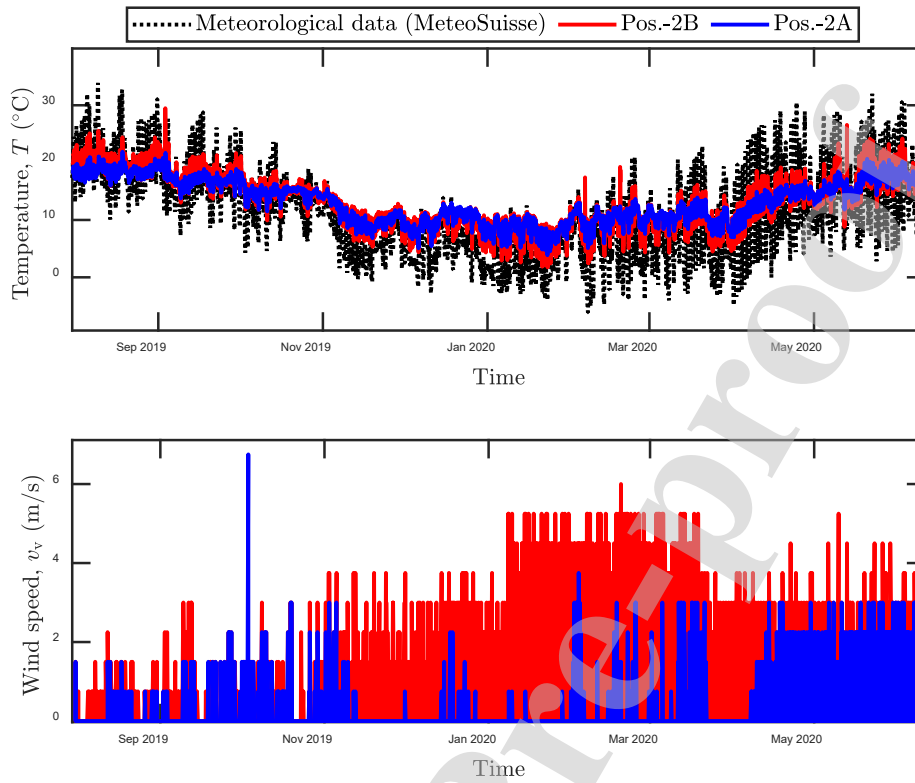
174 This section presents the results related to (i) the hydrothermal behavior of the train station and the  
175 experimental results of the (ii) TRT and (iii) heating/cooling HP tests.

#### 176 3.1. Hydrothermal behavior at the train station level

177 The train station hydrothermal behavior is detailed here with reference to (i) its seasonal temperature  
178 evolution with correlation to the ground surface environmental temperature and (ii) the wind speed  
179 profile and the interactions with the train circulation effects. The monitored results are compared with  
180 the surface temperature measurements taken by Météo Suisse at the Genève Airport weather station.

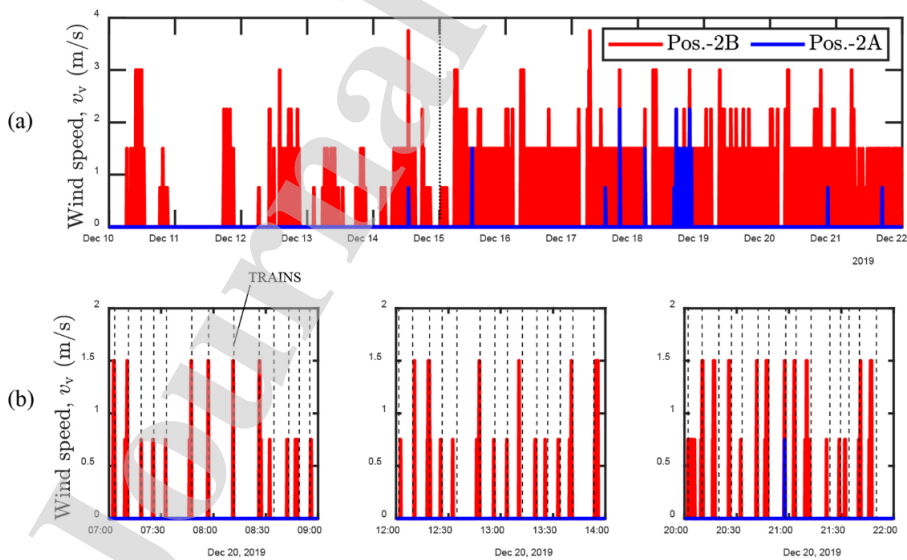
181 From the thermal interactions between the tunnel and ground surface (i.e., external) temperature  
182 evolution, two behaviors are apparent (Figure 3). From August to October and from March to June, the  
183 tunnel temperature follows periodic behavior daily, which is lower than the external temperature during  
184 the day and higher at night. During a period, the average difference between the tunnel and external  
185 temperatures is, in absolute terms, approximately 6.0 °C and 4.0 °C for day and night, respectively. The  
186 tunnel temperature varies between 12.2 °C and 30.1 °C. The external temperature varies between  
187 -2.5 °C and 33.8 °C. The temperature recorded at position -2B is generally higher than that at position  
188 -2A. From the end of October to March, the tunnel temperature behaves periodically on a daily basis  
189 and is always (i.e., during day and night) higher than that recorded outside. The difference between the  
190 tunnel temperature and external temperature varies between 3 ÷ 5 °C. The tunnel temperature varies  
191 between 6.5 °C and 13.0 °C. The external temperature varies between -5.5 °C and 13.1 °C. The  
192 minimum values are lower at position -2B than at -2A.

193 The wind speed profile (Figure 3) shows two behaviors, occurring before and after the start of train  
194 traffic circulation (i.e., on December 15<sup>th</sup>, 2019, Figure 4(a)). Before the start of train traffic circulation,  
195 wind speed values greater than 0.5 m/s (i.e., the lower operational limit of the instrument) are recorded  
196 sporadically. A limited difference between the values measured at positions -2A and -2B is reported.  
197 After the start of train traffic circulation (Figure 3 and Figure 4), more frequent wind speeds higher than  
198 the thresholds are recorded. This behavior is described in detail in Figure 4, which reports the overall  
199 airflow behavior before and after the beginning of train circulation (Figure 4(a)), denoting periodic daily  
200 behavior after December 15, 2019. Figure 4 (b) shows the correlation between air speed measurements  
201 and the passage of trains at three times of a typical day (i.e., morning, afternoon, evening). The peaks  
202 of the air speed values coincide perfectly with the train passages, which were taken by studying the  
203 train timetable available at the train station.



205

Figure 3 Tunnel air temperature evolution and wind speed from the end of July 2019 to the beginning of June 2020



207

Figure 4 Measurement of wind velocity: (a) global view of the behavior before and after the beginning of train circulation (i.e., on Dec. 15); (b) magnified view at three times during a typical day after train traffic circulation starts and correlations between the wind speed measurements and train passages

208

209

210

### 211 3.1.1. Definition of the yearly temperature profiles near the underground 212 energy infrastructure

213 The measurements allow us to reconstruct the yearly temperature profiles in the environments located  
214 near the UEI that affect thermal exploitation. These values, which are summarized in Table 2, are also  
215 used as boundary conditions for the numerical model that simulates the in situ tests, as presented in  
216 section 4.

217

Table 2 Determination of the yearly temperature profiles for each boundary condition

	External temperature (ground surface)	Tunnel temperature	Technical room temperature
	$T_{gs}$ (°C)	$T_t$ (°C)	$T_{tr}$ (°C)
Jan	2.2	6.0	11.0
Feb	2.9	8.0	10.0
Mar	6.9	11.0	12.0
Apr	11.0	15.0	13.5
May	14.7	18.5	17.0
Jun	19.2	21.0	19.0
Jul	20.8	22.0	21.0
Aug	20.0	21.0	21.0
Sep	16.0	18.5	18.5
Oct	11.7	15.0	16.0
Nov	6.4	11.0	13.5
Dec	2.9	8.0	11.5

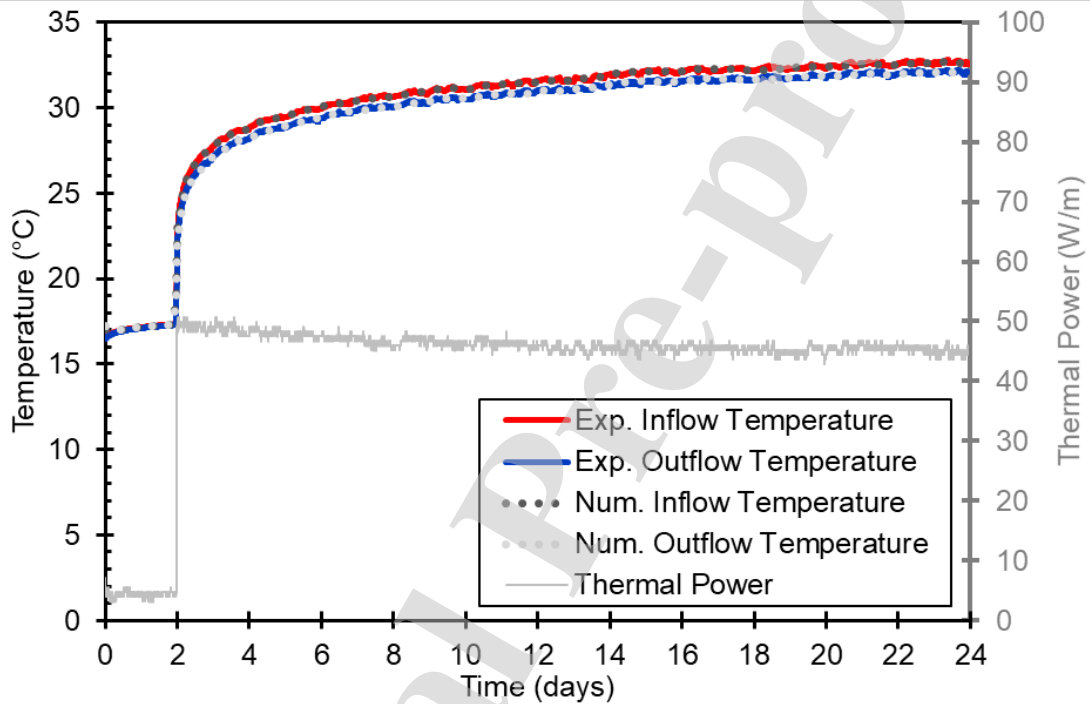
218

### 219 3.2. TRT

220 The test started with a fluid circulation phase (i.e., no heating), which lasted 2 days. The duration was  
221 chosen after running a preliminary test a few weeks in advance, with a duration of one week, that  
222 showed no fluid temperature fluctuations on a day/night basis. The heat injection phase at constant  
223 power lasted 24 days, which is considered sufficient to reach the steady state.

224 During the fluid circulation phase, the fluid temperature reached a constant value of  $T_{f,exp} = 17.3$  °C,  
225 which represents the average temperature of the wall subjected to the effects linked to the soil, tunnel  
226 and ground surface temperatures (Figure 5). This value is slightly higher than the average soil

227 temperature values recorded for European climates (Mattsson et al., 2008; Pahud & Matthey, 2001;  
 228 Rotta Loria & Laloui, 2017a), suggesting that the soil temperature distribution could be affected by the  
 229 presence of the tunnel. During the heating phase (i.e., application of constant power), the fluid  
 230 temperature rapidly increased. Two distinct periods are clearly distinguished: an initial, transient phase  
 231 of approximately 5 ÷ 7 days is followed by a steady state condition, in which the fluid temperature  
 232 slowly increases with time (Figure 5). The temperature difference between the inflow and outflow  
 233 remains constant throughout the heating phase and is equal to  $\Delta T_f = 0.6 \text{ }^\circ\text{C}$ .



235 Figure 5 Experimental data from the TRT module (fluid temperature and thermal power) with fitting of the numerical results

236

### 237 3.3. Heat pump tests

238 To test the UEI behavior under realistic heating/cooling operation modes, additional tests were  
 239 executed. The equipment used during these tests consists of a water-to-air heat pump (HP) located at  
 240 level -1, which replaces the TRT module. A dedicated hydrothermal monitoring system is designed for  
 241 this installation. This monitoring system allows for continuous measurement of (i) inflow and outflow  
 242 fluid temperatures,  $T_{f,in}$  and  $T_{f,out}$ , respectively; (ii) the flow rate,  $\dot{V}$ , of the HCF; (iii) the air  
 243 temperature at the HP ventilator,  $T_{ventilator}$ ; and (iv) the technical room temperature,  $T_{tr}$ . Heating and  
 244 cooling tests at constant inflow temperature were executed between December 2019 and March 2020  
 245 to simulate realistic summer and winter operations, respectively. The HP allows for setting a user-  
 246 defined  $T_{f,in}$ , and it automatically sets the time-dependent behavior of the internal circulation pump

247 (i.e., settings of flow rate) to ensure the best functioning and respect for the maximum and minimum  
 248 internal temperatures to avoid any excessive heating and/or fluid freezing.

249 The objectives of these tests are to reach limiting values (maximum and minimum) of the HCF  
 250 temperature representative of future UEI operations. In other words, these tests aim to represent worst-  
 251 case scenarios in terms of the temperature difference imposed on the UEI from a thermomechanical  
 252 viewpoint and best-case scenarios in terms of thermal exploitation (i.e., highest thermal power). In the  
 253 following, the results for heating and cooling tests are reported and discussed.

### 254 3.3.1. Heating tests

255 A heating test was executed in December 2019. The time of year in which the tests were performed was  
 256 imposed by the construction site's tight schedule. Heating tests represent the summer behavior of a UEI:  
 257 heat is injected in the ground to produce fresh air used for air conditioning of the superstructure. The  
 258 heating test performed in this context aims at achieving high temperature levels in the range of values  
 259 normally used in low enthalpy geothermal applications and for heat storage operations (Gao et al., 2015;  
 260 Gehlin, 2016; Nordell et al., 2015; Reuss, 2015; Witte & Van Gelder, 2007). During heating tests (i.e.,  
 261 summer operation), the HCF is therefore cooled by exchanging heat with the surrounding materials,  
 262 which are at a lower temperature than that imposed by the heat pump. As a result, the wall and soil are  
 263 heated. Finally, the heat pump, via its refrigerating internal cycle, produces fresh air.

264 Heat injection at constant temperature was performed by fixing  $T_{f,in} = 50.0$  °C. The observed HP  
 265 behavior is continuous and cyclic (Figure 6 (a)), with approximately 2 cycles per hour. The heat pump  
 266 is switched on for approximately 15 minutes, when  $T_{f,in}$  increases to the set value, and then for  
 267 approximately 15 minutes,  $T_{f,in}$  gently decreases to allow for thermal recharging around the HEs.  
 268  $T_{f,in}$  varies between  $45.0 \div 56.5$  °C.  $T_{f,out}$  varies accordingly, with a slight time shifting of a few  
 269 seconds. The average HCF temperature variation between the outflow and inflow is  $\Delta T_f = T_{f,in} -$   
 270  $T_{f,out} = 5.9$  °C. The flow rate varies between  $\dot{V}_f = 18 \div 27$  L/min. The average thermal power  
 271 injected (i.e., negative) by HP operation is  $Q_{th,f} = -7$  kW. A global view of the heating test is provided  
 272 in Figure 7(a).

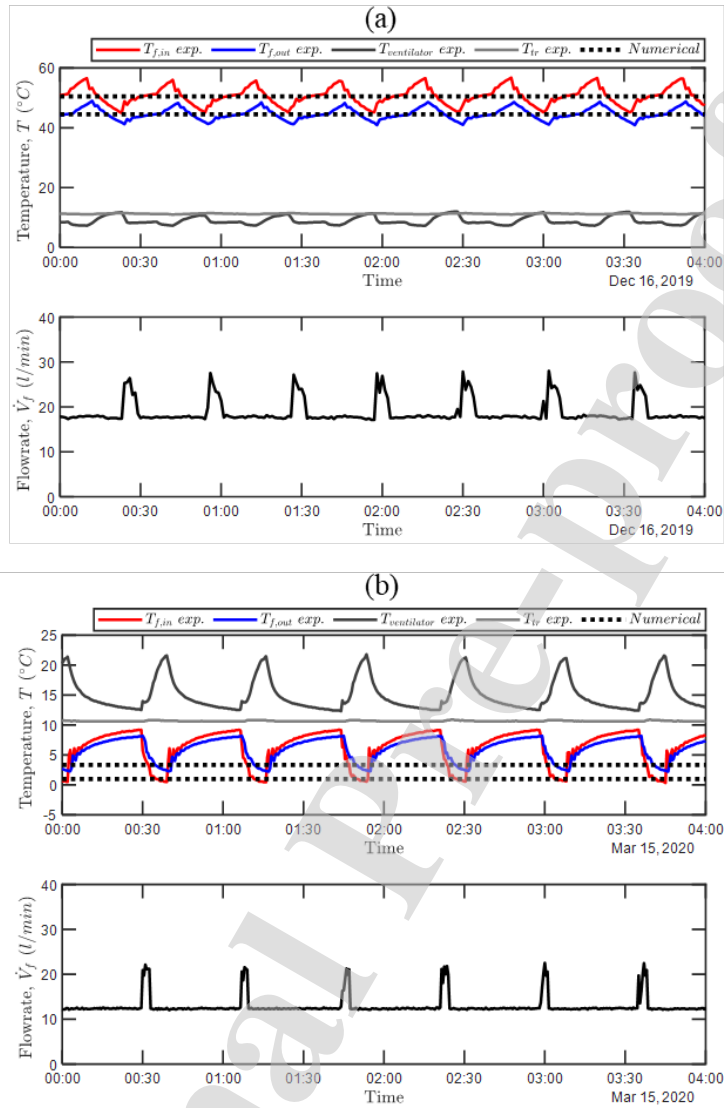
273

### 274 3.3.2. Cooling test

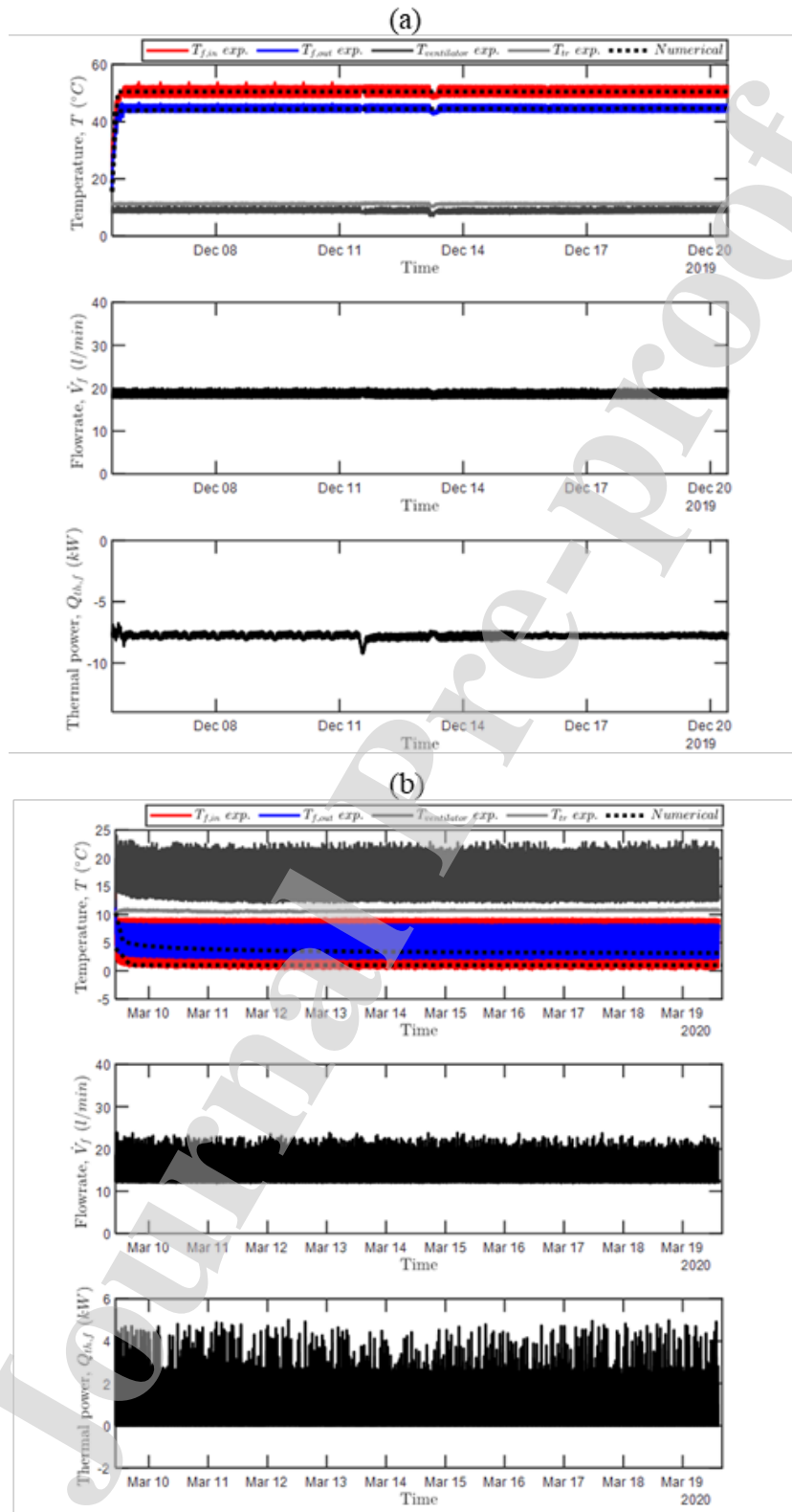
275 A cooling test was performed in March 2020. The cooling test represents the winter behavior of a UEI:  
 276 a cold HCF is injected into the HEs, and by extracting heat from the surroundings, the fluid is heated  
 277 until the outlet point. It follows that the materials within the UEI (i.e., pipes, wall, soil and tunnel) are  
 278 cooled as heat is extracted by the HCF. During this operation, the HP produces hot air for heating the  
 279 superstructure. The cooling test performed here aims at achieving the lowest values of HCF temperature  
 280 allowable by the HP, simulating a real winter operation (Adam & Markiewicz, 2009; Batini et al., 2015;

281 Brandl, 2006; Di Donna, 2016; Kavanaugh & Rafferty, 2014; Loveridge et al., 2020; Makasis &  
282 Narsilio, 2020; Shafagh et al., 2020; Sterpi et al., 2018; Zannin et al., 2020).

283 The inflow temperature was set to  $T_{f,in} = 1.0$  °C. The heat pump response was highly discontinuous on  
284 a periodic basis (Figure 6 (b)). The HP switched on for a limited period (i.e., approximately 25 minutes  
285 per hour) and then switched off, stopping the imposition of the inflow temperature but allowing the  
286 fluid to circulate at ambient temperature. In this way, temporary thermal recharge of the materials  
287 surrounding the HCF was possible, and heat extraction could afterwards resume. This strongly  
288 intermittent, periodic behavior occurred because the minimum allowable HCF temperature value was  
289 reached, and the HP needed to stop to avoid freezing issues. The inflow temperature ranged between  
290  $T_{f,in} = 0.5 \div 9.2$  °C. The outlet temperature varied between  $T_{f,out} = 2.3 \div 8.2$  °C. The average inflow-  
291 outlet fluid temperature difference was  $\Delta T_f = 2.5$  °C. The flow rate ranged between  $\dot{V}_f = 12 \div$   
292  $24$  L/min. The average thermal power extracted (i.e., positive) was  $Q_{th,f} = 2$  kW. A global view of  
293 the cooling test is shown in Figure 7(b).



295 Figure 6 Magnified view of HP behavior during different cycle types: (a) heating test, December 2019 and (b) cooling test,  
 296 March 2020



298  
299

Figure 7 Global view of the HP behavior during the experiments: (a) heating test (December 2019) and (b) cooling test (March 2020)



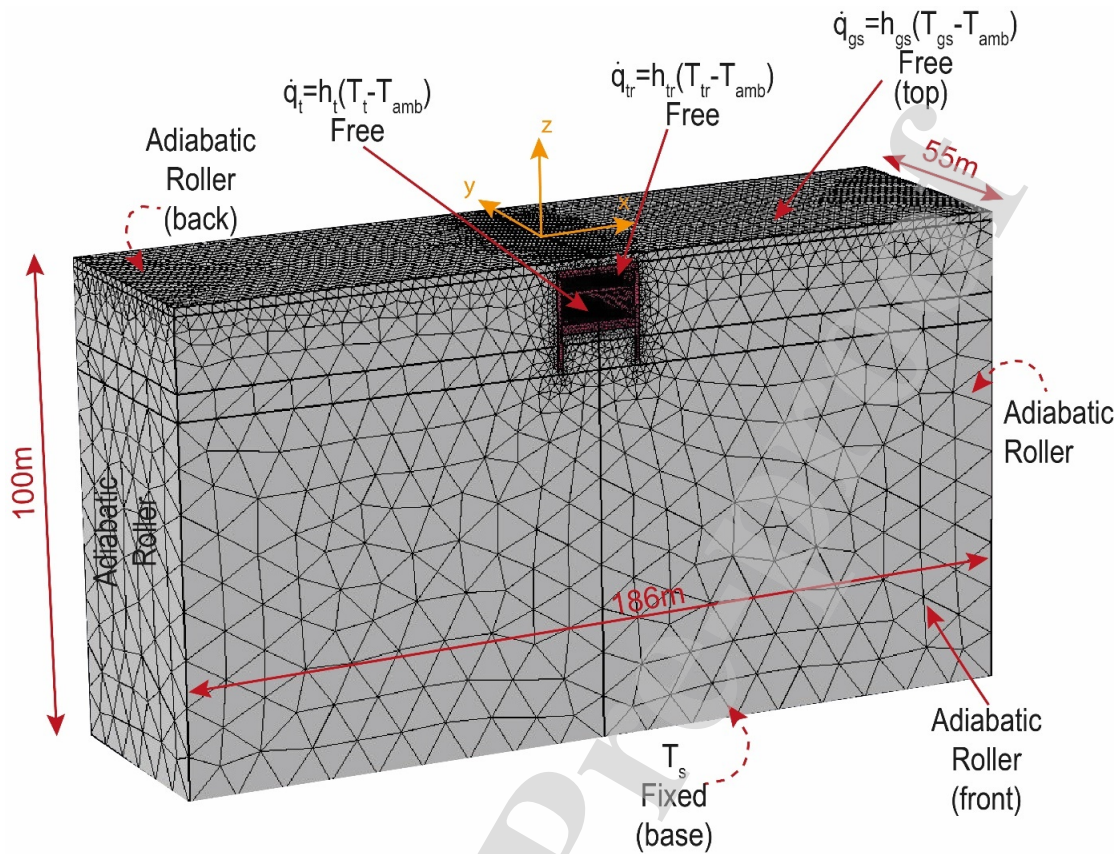
300

## 301 4. Hydrothermal behavior: numerical modeling

## 302 4.1. Features of the numerical analyses

303 A 3D finite element model (i.e., thermomechanical, featuring for the non-isothermal fluid flow in the  
304 HE) used to simulate the in situ test and to interpret the results is built using the software COMSOL  
305 Multiphysics (COMSOL Inc., 2018).

306 The objectives for the numerical analyses are (i) to help determine the thermal characteristics of the  
307 materials involved in the heat exchanges; (ii) to give a comprehensive overview of the hydrothermal  
308 behavior of the UEI, highlighting the soil temperature distribution before and during the tests, the  
309 volume of materials affected by the thermal exchanges, and the direction and magnitude of the wall-  
310 tunnel and wall-soil heat fluxes; and (iii) to study the thermomechanical behavior. Some of the  
311 parameters measured experimentally are input parameters for the numerical model (e.g., inflow  
312 temperature and velocity, boundary conditions), while others are back-analyzed to calibrate the  
313 numerical model to best fit the experimental data (e.g., thermal characteristics of materials). The model  
314 dimensions are  $186\text{ m} \times 55\text{ m} \times 100\text{ m}$  in the x-, y-, and z-coordinates (Figure 8). The HEs are modeled  
315 following the technical details of the geostructural design. The soil and structure are modeled as fully  
316 saturated porous materials. The groundwater is considered in stationary condition with null velocity;  
317 hence, convective heat exchanges within the soil are neglected. The mathematical formulation and  
318 details of the numerical model are reported in Appendix A.



320

Figure 8 Geometry of the numerical model with indication of the boundary conditions

321 The thermal boundary conditions (Figure 8) are as follows: the two vertical surfaces at the sides are  
 322 adiabatic (i.e., the far-field temperature distribution with depth is not affected by the tunnel, and the  
 323 surface temperature affects the top 15 m, simulating realistic far-field conditions); the front and rear  
 324 vertical surfaces are adiabatic; the bottom horizontal surface is set to a constant temperature,  $T_s$  (i.e.,  
 325 the soil temperature); and the ground surface, technical room and tunnel air interfaces are simulated by  
 326 means of convective boundary conditions (i.e., flux conditions,  $\dot{q}_i$ ), setting a coefficient for convective  
 327 heat transfer,  $h_i$ , and an air temperature,  $T_i$ , based on experimental results.  $h_i$  is linked to the air velocity  
 328 and is calibrated following the available correlations (Bourne-Webb et al., 2016; Guo et al., 2011; Lee  
 329 et al., 2009; Peltier et al., 2019).  $h_i$  was chosen as  $h_{gs} = 10 \text{ W/m}^2/\text{K}$ ,  $h_{tr} = 3 \text{ W/m}^2/\text{K}$ , and  $h_t = 4$   
 330  $\text{W/m}^2/\text{K}$  for the ground surface, technical room and tunnel, respectively; the first coefficient represented  
 331 a wind velocity of approximately 1 m/s, and the latter coefficients represented a “quasi-zero” wind  
 332 velocity.  $T_i$  are transient functions set as in Table 2. The mechanical boundaries are as follows: the base  
 333 boundary is fixed, and all the vertical boundaries are rollers, while the remaining boundaries are free  
 334 (Figure 8). The nonisothermal fluid flow in the HE is simulated by imposing the experimental time  
 335 history of fluid inflow temperature and velocity, while the outflow fluid temperature is used to calibrate  
 336 the model with respect to the experimental results. The solver accounts for a temperature initialization  
 337 phase of 10 years duration to ensure that the result is independent of the model initial condition,

338 followed by simulating the experimental tests. During such period, the periodic thermal boundary  
 339 conditions (Table 2) are applied so that to obtain a realistic temperature initialization before the start of  
 340 geothermal operations. Further outcomes on this aspect are reported in section 4.3.

## 341 4.2. TRT

342 The objectives of numerical modeling are to interpret the experimental results, giving a full picture of  
 343 the hydrothermal aspects involved in UEI operation. The TRT is usually employed in geothermal  
 344 applications (Bourne-Webb et al., 2016; Loveridge et al., 2020, 2015; Sanner et al., 2005; Shafagh et  
 345 al., 2020; Zannin et al., 2019) to thermally characterize the materials surrounding a thermoactive  
 346 element (e.g., borehole, pile), determining (i) the undisturbed soil temperature and (ii) the average  
 347 thermal conductivity of the soil. Numerical techniques are adopted instead of, for example, analytical  
 348 and/or semianalytical techniques for addressing these challenges because of the geometrical  
 349 complexities and the highly transient thermal behavior of the UEI and its boundary conditions (Figure  
 350 3, Table 2).

351 The undisturbed soil temperature,  $T_s$ , is varied to obtain an average temperature in the HEs equal to that  
 352 measured by the TRT module during the water circulation phase. This correspondence occurs for  $T_s =$   
 353 14.6 °C, which is consistent with the expected values for the European climate. Before the start of the  
 354 heating phase of the TRT, the average fluid temperature is  $T_{f,num} = 17.30^\circ\text{C}$ , which is very close to  
 355 the experimental value,  $T_{f,exp} = 17.34$  (Figure 5).

356 The estimate of the thermal characteristics of the involved materials (i.e., soil and concrete) represents  
 357 the second objective. To do so, an issue related to the unicity of the solution exists: it is impossible to  
 358 uniquely determine the thermal conductivity of soil and concrete while having only one experimental  
 359 result. Concrete thermal conductivity could realistically vary between  $\lambda_c = 1.0 \div 2.0$  W/m/K (Asadi et  
 360 al., 2018; Bourne-Webb et al., 2016; Valore, 1980; Zhang et al., 2015). Soil thermal conductivity (i.e.,  
 361 normally consolidated clay and slightly overconsolidated clay in saturated conditions) could  
 362 realistically be evaluated as  $\lambda_s = 1.0 \div 2.5$  W/m/K (Laloui & Rotta Loria, 2019; Vulliet et al., 2016).

363 Dedicated parametric studies are run to detect the impact of thermal capacity of soil and concrete in  
 364 reproducing the experimental results. Thermal capacity plays a role during the transient phase of the  
 365 TRT heating, which lasts approximately 2 days (Figure 5). Then, the process is driven by thermal  
 366 conductivity as a steady-flux condition is reached. Such analyses highlighted that very marginal effects  
 367 are played by thermal capacity of concrete and soil. For such reasons, thermal capacity and density are  
 368 fixed to  $Cp_c = 850$  J/kg/K,  $\rho_c = 2722$  kg/m<sup>3</sup>,  $Cp_s = 1000$  J/kg/K, and  $\rho_s = 2011$  kg/m<sup>3</sup> for concrete  
 369 and soil, respectively (Laloui & Rotta Loria, 2019; Vulliet et al., 2016; Zannin et al., 2019; Bourne-  
 370 Webb et al., 2016). A sensitivity analysis of thermal capacity effects was performed, showing little  
 371 variation in the UEI thermal performance. Concrete thermal conductivity was fixed to different values,  
 372 and soil thermal conductivity was evaluated to best match the experimental results (Table 3). The  
 373 comparison between the experimental and numerical results was performed at the outflow fluid

374 temperature,  $T_{f,out}$ , which is not an input parameter of the numerical model. The error is evaluated as  
 375  $T_{f,out,num} - T_{f,out,exp}$ , as reported in Table 3. In the following, the numerical results for  $\lambda_c = 1.7$   
 376 W/m/K and  $\lambda_s = 1.4$  W/m/K are reported, as they represent the best fitting to the experimental results.  
 377 Close agreement between the experimental and numerical results is reported in Figure 5.

378

379 Table 3 Evaluation of thermal conductivity for concrete and soil: determination of soil thermal conductivity to best match  
 380 the experimental results for a given concrete thermal conductivity

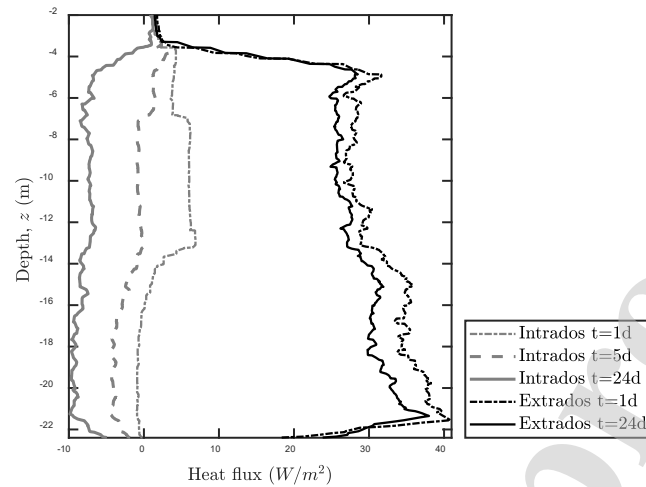
Concrete thermal conductivity $\lambda_c \left( \frac{W}{mK} \right)$	Soil thermal conductivity $\lambda_s \left( \frac{W}{mK} \right)$	Absolute numerical-experimental error at steady state ( $^{\circ}C$ )
1.7	1.4	0.014
1.5	1.9	0.026
1.2	2.1	0.044
1.0	2.4	0.045

381

382 Additionally, numerical analyses give a broader view of the thermal response of the UEI during TRT  
 383 execution, with emphasis on (i) the temperature profile of the materials upon heating, (ii) heat fluxes  
 384 and (iv) intrados tunnel temperature.

385 At the beginning of the heating phase, the soil is strongly affected by thermal exchanges because of the  
 386 vicinity of the HE: consequently, the heat exchanger-soil heat flux (i.e., extrados) slightly decreases  
 387 with time due to heat propagation in the soil and the increase in the soil volume affected by temperature  
 388 variations. The extrados heat flux range is between  $25 \div 35$  W/m<sup>2</sup> (Figure 9). At the end of the test, the  
 389 model suggests that a soil portion of thickness 1.5 m around the EW is affected by a temperature  
 390 variation of  $> 1^{\circ}C$  with respect to its initial temperature distribution.

391 The temperature distribution inside the concrete geostructure evolves with time. At the beginning of  
 392 heating and during a portion of the transient condition, the intrados temperature is higher than that of  
 393 the HCF. It follows that the heat flux is directed from the tunnel toward the HCF. The tunnel, in this  
 394 phase, acts as a thermal resistance rather than as a conductor (Figure 9), where a positive heat flux  
 395 denotes a flux vector directed toward the positive x-axis (i.e., from the wall toward the soil). The tunnel  
 396 is located between  $z = -7.5$  m and  $z = -14$  m, and a positive heat flux with a magnitude of  
 397 approximately  $+7.5$  W/m<sup>2</sup> is recorded. When the HCF temperature increases, it becomes higher than  
 398 that of the tunnel, hence reversing the heat flux. It reaches its stationary condition at approximately  $-10$   
 399 W/m<sup>2</sup>. The heat fluxes are hence dominated by the extrados component, which is  $3 \div 5$  times higher  
 400 than the intrados component.



402 Figure 9 Magnitude of heat flux at the wall intrados and extrados

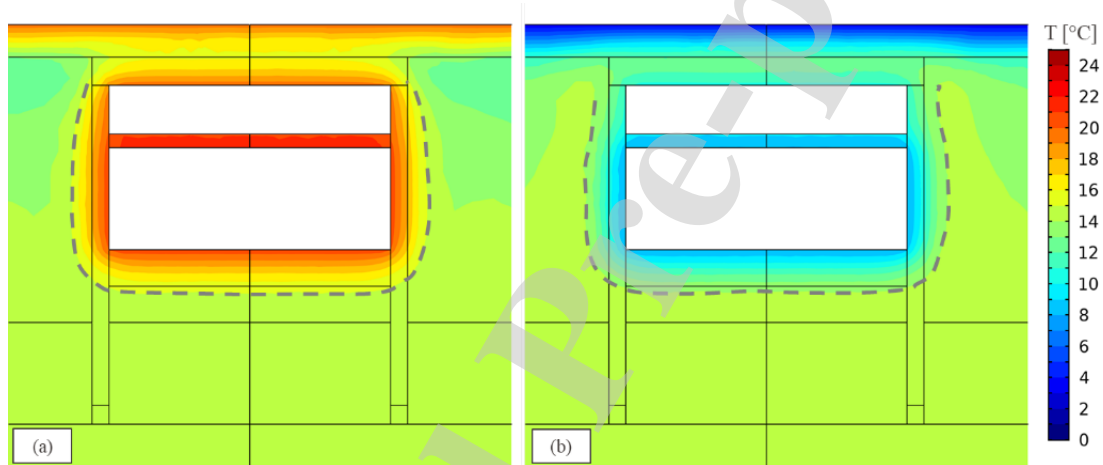
403 Thermal photos at level -2 were taken on the last day of testing and compared with the numerical results,  
 404 showing close agreement (complementary results are available in Zannin (2020)). The longitudinal  
 405 thickness of the intrados thermally affected zone is 2.5 m. The intrados temperature varied between  
 406  $20 \div 22$  °C on 21/08/2019 and between  $20 \div 23$  °C on 29/08/2019. It follows that the temperature  
 407 distribution inside the wall is nonuniform: it shows a maximum located near the HCF. The temperature  
 408 decreases until reaching a minimum at the wall-tunnel interface.

#### 409 4.3. Heat pump tests

410 The heat pump tests are numerically simulated using the same model presented above. Inflow  
 411 temperature is imposed as the average monitored  $T_{f,in}$ , while the outflow temperature is used for  
 412 comparison among the numerical and experimental results. To reduce the computational cost, the  
 413 numerical model cannot capture each HP cycle, but the average inflow and outflow temperatures are in  
 414 close agreement with the experimental results for the heating (Figure 6(a)) and cooling (Figure 6(b))  
 415 tests.

416 Before analyzing the details of the wall-tunnel interactions during the thermal activation tests, it is worth  
 417 analyzing the UEI-tunnel interactions induced by the application of boundary conditions only. As  
 418 reported in Table 2, the temperature profiles at the boundaries present yearly periodic behaviors. These  
 419 conditions have implications on the UEI operation, as they modify the temperature profile of the UEI  
 420 itself and its surroundings. A portion of the wall and soil undergoes a seasonal temperature variation of  
 421  $\Delta T \cong 6 \div 10$  °C (Figure 10). The concrete presents maximum/minimum temperatures of  $T_c = 19 \div$   
 422  $9$  °C during summer and winter. The soil (i.e., the portion within the dashed gray lines reported in Figure  
 423 10) presents  $T_s = 17 \div 11$  °C during summer and winter. These temperature variations must be  
 424 considered when studying UEI operation for two reasons. First, temperature variations induced by  
 425 natural effects on the order of magnitude of several degrees Celsius may affect the validity of the

426 hypothesis of “yearly constant soil temperature”, which is often applied to energy geostructures (Laloui  
 427 and Rotta Loria, 2019). Second, Figure 10 shows that the portion of materials that undergoes these  
 428 temperature variations represents more than 50% of the volume of the most thermally affected materials  
 429 during UEI operation. It follows that these environmental temperature variations will affect the UEI  
 430 operation, as the tunnel heats the materials during summer and cools them during winter, reducing the  
 431 seasonal potential for heat injection and extraction, respectively. This reduction is already partly  
 432 apparent in the HP results for the cooling test (section 3.3.2), as the heat pump must periodically stop  
 433 to allow for thermal recharge before resuming its operation. This effect is detrimental to winter  
 434 operation: a reduction in the average temperature of materials reduces the potential for cooling the UEI,  
 435 as the allowable operative temperature range is already limited from most operative prescriptions and  
 436 available standards (CFMS-SYNTEC-SOFFONS-FNTP, 2017; GSHPA, 2012; SIA D0190, 2005).

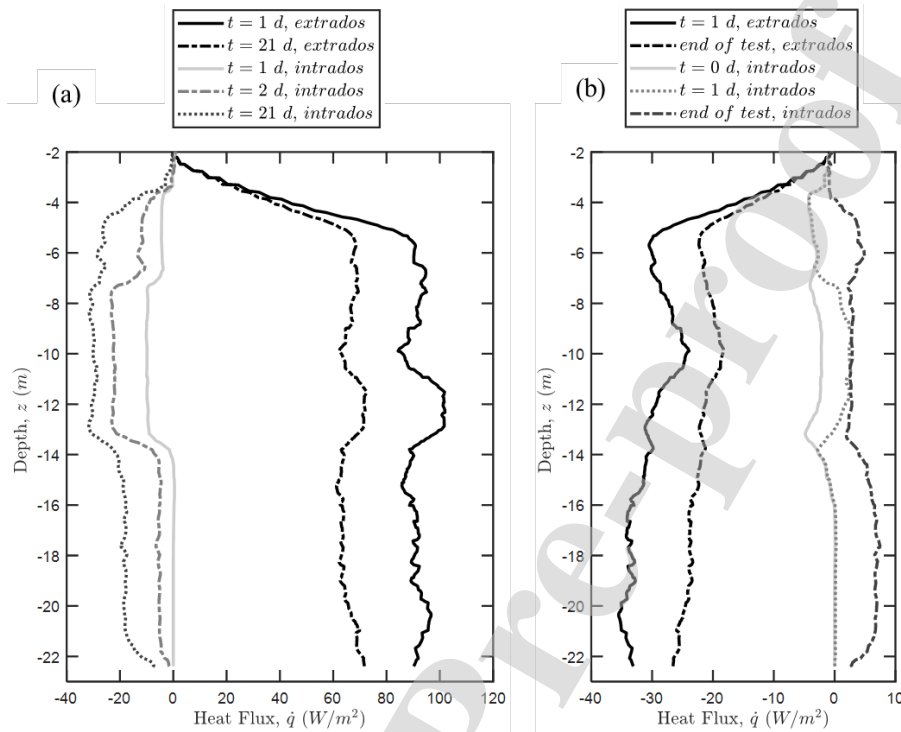


438 Figure 10 Temperature profile (numerical results) within and around the UEI determined by applying the tunnel, technical  
 439 room and surface boundary conditions: (a) summer and (b) winter. The dotted gray line denotes the portion of materials that  
 440 undergoes the most severe temperature variations induced by applying boundary conditions.

441 Analyses of the hydrothermal behavior during heating and cooling tests are reported here. Upon heating,  
 442 the maximum portion of materials affected by thermal effects extends up to 2 m of soil laterally to the  
 443 UEI. The maximum wall temperature is  $T_{w,max} = 38.0$  °C. The magnitude of the intrados heat fluxes  
 444 is transient. The wall and tunnel act as conductors, with the heat flux magnitude increasing as the heating  
 445 persists. The extrados heat flux strongly dominates the intrados heat flux (Figure 11(a)). The heat flux  
 446 at the extrados is slightly higher for the top portion of the wall (i.e., facing the tunnel level) than for the  
 447 bottom portion because the initial soil temperature is lower. The magnitude of the heat flux at the  
 448 extrados is thrice that at the intrados.

449 Upon cooling, the portion of materials affected by thermal effects extends up to 1 ÷ 1.5 m of soil  
 450 laterally to the UEI, with the portion of soil affected by thermal effects increasing in volume as the  
 451 cooling persists. The minimum wall temperature is  $T_{w,min} = 4.3$  °C. The heat flux at the extrados is  
 452 higher in the fully embedded portion of the wall than at the top part, contributing to the higher

453 temperature difference between the soil and the HCF (Figure 11(b)). The magnitude of the heat flux at  
 454 the extrados is fivefold higher than that at the intrados.



456 Figure 11 Intrados and extrados heat fluxes: (a) heating test and (b) cooling test

457 The wall intrados is affected by temperature variations induced by the thermal activation of the UEI.  
 458 Comparisons between experimental (i.e., thermal photos) and numerical results showed close  
 459 agreement (complementary results are available in Zannin (2020)). Upon heating, the longitudinal  
 460 extent of the intrados' thermally affected region was 2.5 m. The average temperature difference  
 461 between the thermally affected and undisturbed portions was 3.5 °C. Upon cooling, the longitudinal  
 462 extent of the thermally affected portion was 1 m. The average temperature difference between the  
 463 thermally affected and undisturbed regions was -1.5 °C. Close agreement between the experimental  
 464 and numerical results was found (Zannin, 2020).

#### 465 4.4. Preliminary guidelines for TRT execution and data interpretation for 466 underground thermoactive infrastructures

467 This section discusses the details of the execution of TRTs applied to UEIs and, more generally, to any  
 468 geostructure partly in contact with an air interface. To our knowledge, no literature on this topic is  
 469 available. Moreover, no feedback, execution manuals or legislative standards for test execution or data  
 470 interpretation are available.

471 TRT-type heating input was extensively used to determine the soil thermal characteristics for vertical  
472 HEs (Gehlin 2002; Mattsson et al., 2008) and energy piles and to detect the thermomechanical behavior  
473 of energy geostructures (Mimouni & Laloui, 2015; Rotta Loria & Laloui, 2017a, 2017b). Consequently,  
474 the first challenge was to understand what knowledge the execution of TRT on UEIs could bring,  
475 knowing that the focus should be on determining the thermal behavior and potential of the UEI. On the  
476 basis of the foregoing presented results, the main feedbacks are reported here.

477 First, one should verify that the following criteria are fulfilled when performing the test: (i) the fluid  
478 circulation phase should last long enough so that possible day/night fluid temperature variations are  
479 recorded; (ii) the heating phase should last long enough so that the steady state condition within the HE  
480 is successfully reached. In this regard, the typical heating duration used for vertical HEs (i.e., one week)  
481 should be taken as a lower boundary. The longer and/or the more complex the heat exchanger circuit  
482 is, the longer the heating phase should be to ensure that it reaches the steady state. Additionally, the  
483 stronger the hydrothermal interactions with neighboring environments (e.g., air interfaces) are, the  
484 longer the time needed to reach steady state conditions is. (iii) The interpretation of the results requires  
485 a detailed, time-dependent knowledge of the thermal environment characterization near the UEI. The  
486 definition of the initial temperature profile within and around the UEI is crucial. (iv) If the thermal  
487 environments around the UEI are not known with sufficient accuracy, the installation and use of a  
488 dedicated in situ monitoring system is strongly advised. (v) The interpretation of the results should  
489 account for all **relevant** heat exchange modes occurring within and around the UEI. Consequently, the  
490 use of numerical models seems to be the most accurate tool in view of the presence of geometric  
491 complexities. Attempts to determine the soil thermal conductivity using analytical models (Carslaw and  
492 Jaeger, 1952; Mattsson et al., 2008) were made in the case presented in this study. **The multiple,  
493 concurrent, thermal processes lead to a complex definition of the heat fluxes direction, and make the  
494 assumptions of the simplified analytical models unsuitable for the analysis of the geometry in question  
495 (e.g., infinite line source, cylindrical source method, etc...). Thus, there is a need to employ modelling  
496 techniques allowing for a detailed understanding of such heat exchanges. Numerical modelling (FEM)  
497 is a suitable choice.**

498 Finally, it can be concluded that this in situ test allows for replying to the challenge of determining the  
499 thermal characteristics of the involved materials if a correct assessment and monitoring (where needed)  
500 of the relevant boundary conditions is thoroughly performed.

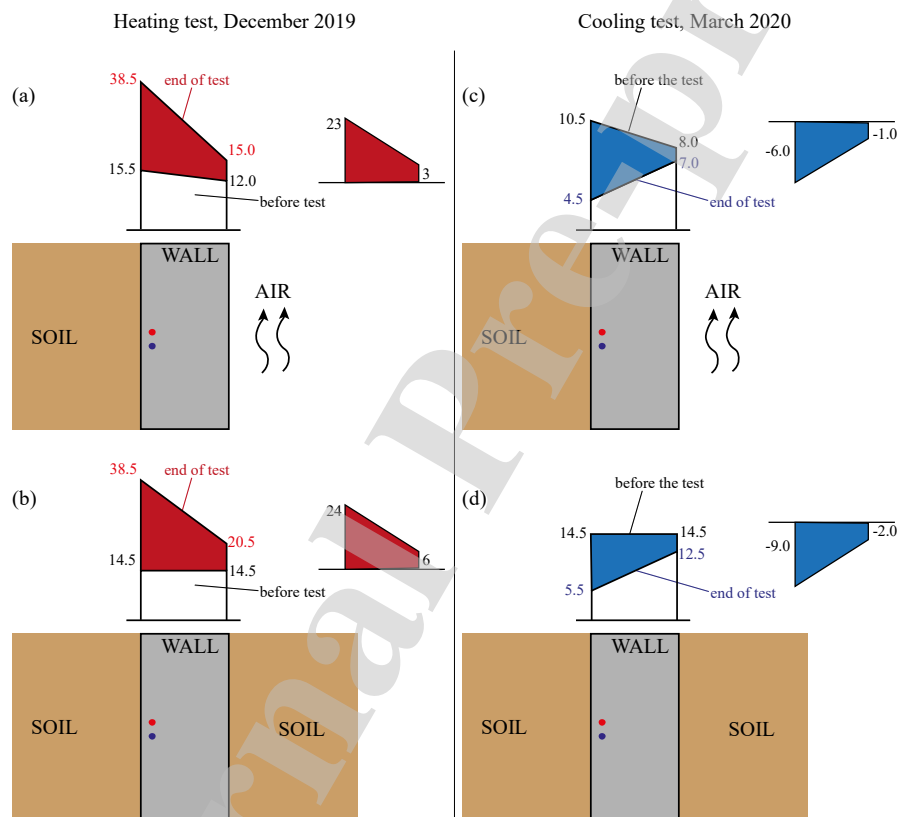
501

## 502 5. Thermomechanical behavior

503 The temperature variations to which the wall is subjected during heating/cooling tests induce  
504 thermomechanical effects in the geostructure. Given that the EW is in contact with different materials  
505 (i.e., concrete slabs, soil, air), different local behaviors are expected at different locations. The contact  
506 with solid materials partly constrains thermally induced deformations (i.e., low degree of freedom,



507 *DOF*, (Rotta Loria et al., 2020; Zannin, 2020; Zannin et al., 2020c)), while at the air interface, the UEI  
 508 has more freedom to deform (i.e., higher *DOF*). On the basis of the experimental and numerical results  
 509 (see Appendix A for the model details), two temperature profiles in the EW are detected. At the top  
 510 portion, the presence of air helps maintain a low temperature variation at the intrados. The air “washes  
 511 away” the temperature difference imposed by the HEs. It follows that the EW temperature variation  
 512 distribution is strongly nonuniform, with an absolute maximum located at the wall-soil interface and a  
 513 minimum at the intrados. At the bottom, in the fully embedded portion, a less pronounced nonuniform  
 514 temperature profile is numerically recorded as a consequence of the nonsymmetrical HE location  
 515 (Figure 12).



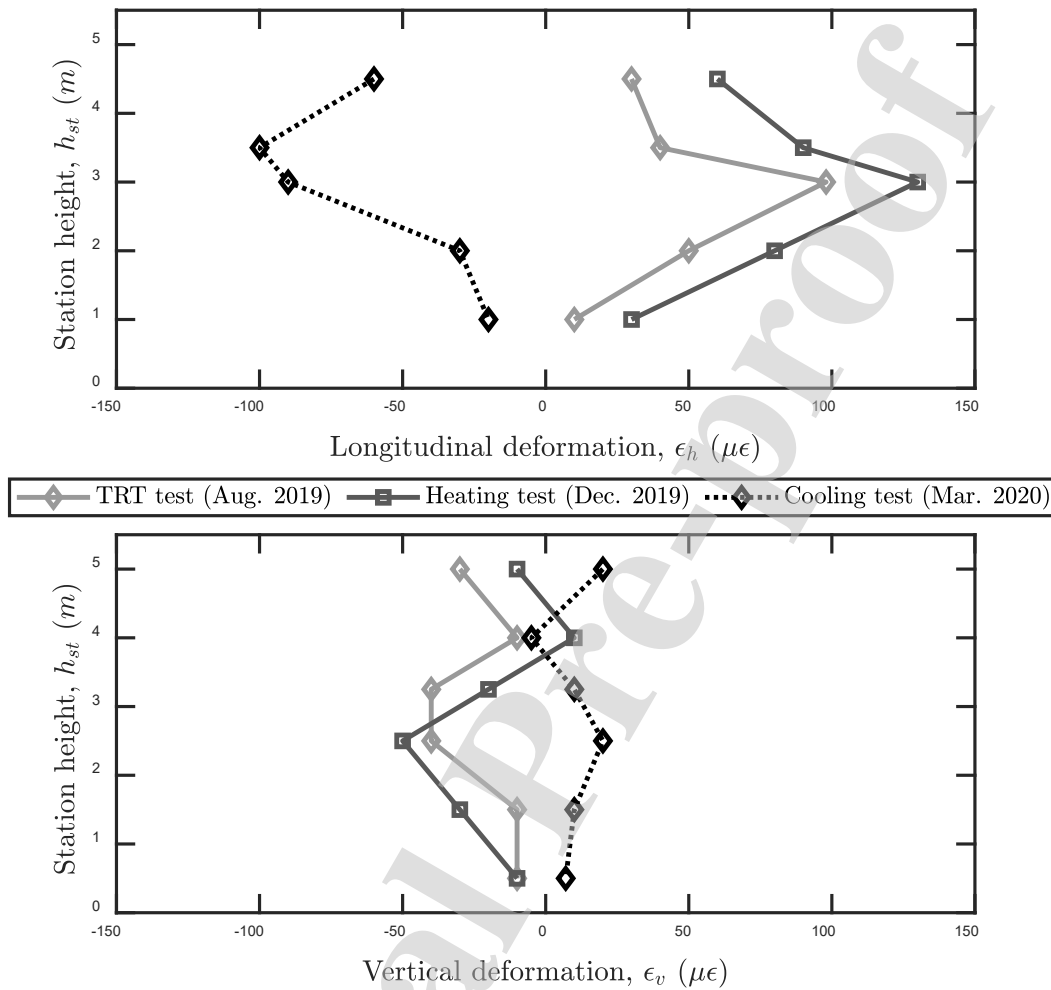
517 Figure 12 Sketches of the temperature distributions in the wall: (a) upon heating, at the top part, facing the tunnel; (b) upon  
 518 heating, at the fully embedded portion; (c) upon cooling, at the top part, facing the tunnel; and (d) upon cooling, at the fully  
 519 embedded portion. The presented values are retrieved from experimental (where applicable) and numerical results. NOTE:  
 520 the sketches are not scaled

521 The monitoring system detailed in section 2.2 is used here to evaluate the wall intrados mechanical  
 522 behavior during the in situ tests. This monitoring system can record the axial deformation of the  
 523 instruments, which are installed alternatively in vertical and longitudinal arrangements at the wall  
 524 intrados of level -2 (Figure 2). The results are reported in Figure 13. The geostructure deforms when  
 525 subjected to thermal loads. Deformations are partly restrained by the soil and the structural connections.

526 The experimental results suggest that two distinct mechanisms can be identified: vertical and  
527 longitudinal mechanisms.

528 The temperature variation throughout the EW cross section is nonuniform (Figure 12). Longitudinally,  
529 temperature diffuses (radially from the HEs) in the wall from the vicinity of the HE toward the intrados  
530 and toward the soil. Upon heating, the EW extrados tend to longitudinally dilate, but this dilation is  
531 partly blocked by the soil. Longitudinally, the only constraint to dilation is represented by the soil, and  
532 no wall-slab connections affect the EW behavior at any longitudinal cross section at level -2. It follows  
533 that dilation at the extrados is partly blocked, but following intrados heating, the intrados is free to dilate  
534 ( $DOF_{intrados} > DOF_{extrados}$ ). For this reason, positive (i.e., expansion) longitudinal deformation  
535 values are attained. The maximum longitudinal deformation is recorded at the tunnel mid-height, where  
536 the wall presents the lowest degree of freedom. The maximum recorded deformation value corresponds  
537 to  $\varepsilon_{h,max} = \Delta L/L_0 = 0.013\%$ . The deformation profile is not instantaneous, but it develops with time,  
538 in agreement with the time-dependent thermal diffusion inside the EW. The opposite was recorded upon  
539 cooling (Figure 13).

540 Upon heating, the EW extrados tend to vertically dilate, but this dilation is partly blocked by the  
541 constraints (i.e., soil and structural connections). During heating tests, the extrados is hotter than the  
542 intrados (Figure 12). Treating the EW as a vertical beam and following the hypothesis that, for small  
543 deformations, the beam cross section maintains its planarity and remains orthogonal to the neutral axis  
544 (Euler-Bernoulli theory of beams (Truesdell, 1960)), the extrados tend to vertically dilate and the  
545 intrados tend to contract (Figure 13). Additionally, structural constraints at the top and bottom of level  
546 -2 (i.e., wall-slab connection and additional stiffness offered by the embedded portion of the wall, wall-  
547 slab connection and self-weight of the superstructure at the top) considerably restrain the degree of  
548 freedom of the wall. It follows that vertical intrados deformations are quasi-null, with a tendency of  
549 being negative (i.e., contractive) following the extrados expansion toward the soil side. The contraction  
550 is maximum at the location of the highest  $DOF$  at the mid-height of the wall facing the tunnel. During  
551 heating, the EW intrados vertically deforms, exhibiting a contraction. The opposite is recorded upon  
552 cooling (Figure 13).



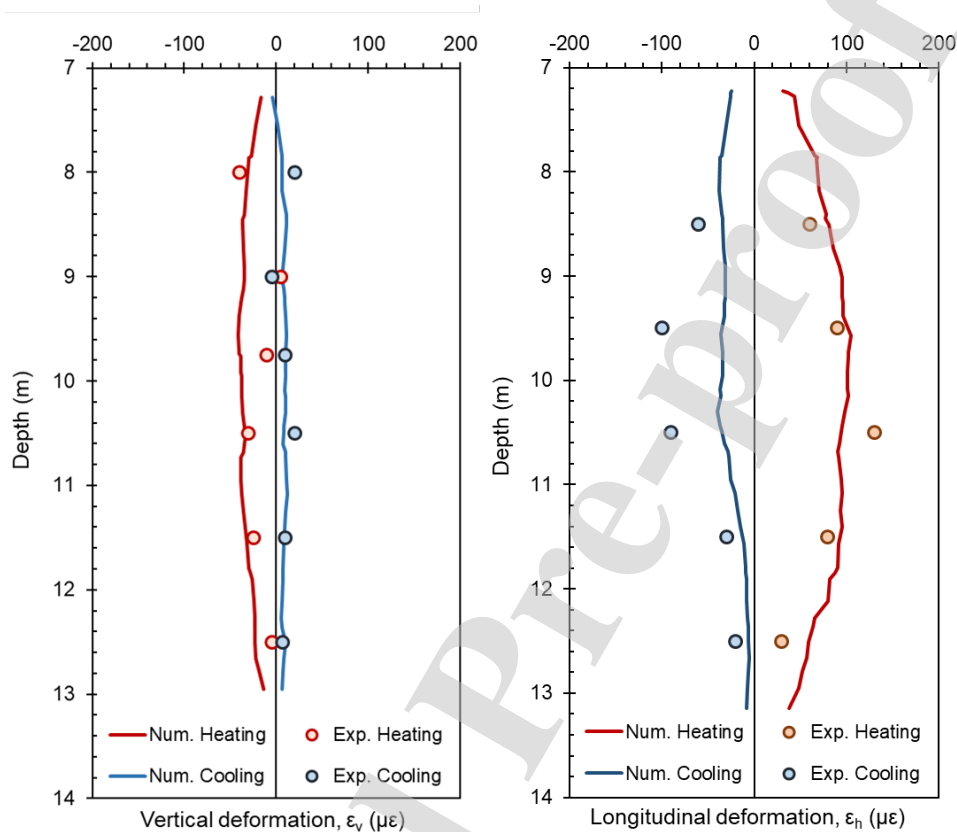
554

Figure 13 Mechanical behavior of the wall intrados facing the tunnel: experimental results

555 These results allow for a qualitative representation of the thermomechanical behavior of the EW. The  
 556 experimental setup used here cannot capture a quantitative and exhaustive definition of the  
 557 thermomechanical wall behavior because of constraints for the sensor's installation (i.e., a monitoring  
 558 system could not be installed at the extrados). The results reported in the present study are consistent  
 559 with those reported on an energy piled wall in Vienna by Brandl (2016), which show maximum seasonal  
 560 relative strains up to  $200 \mu\epsilon$ , located toward the mid-height of the underground tunnel. However,  
 561 limited details are available in (Brandl, 2016) on the experimental setup, making any attempt at a more  
 562 detailed comparison difficult.

563 To estimate the intensity of internal actions and to check the mechanical stability of the UEI, a detailed  
 564 comparison accounting for thermal and mechanical load combinations is performed through 3D finite  
 565 element thermohydronechanical numerical analyses. A comparison among the experimental and

566 numerical results is first performed accounting only for thermal loads by simulating the heating and  
 567 cooling tests. The results of this comparison, referring to the tunnel intrados deformations, are reported  
 568 in Figure 14 and show close agreement.



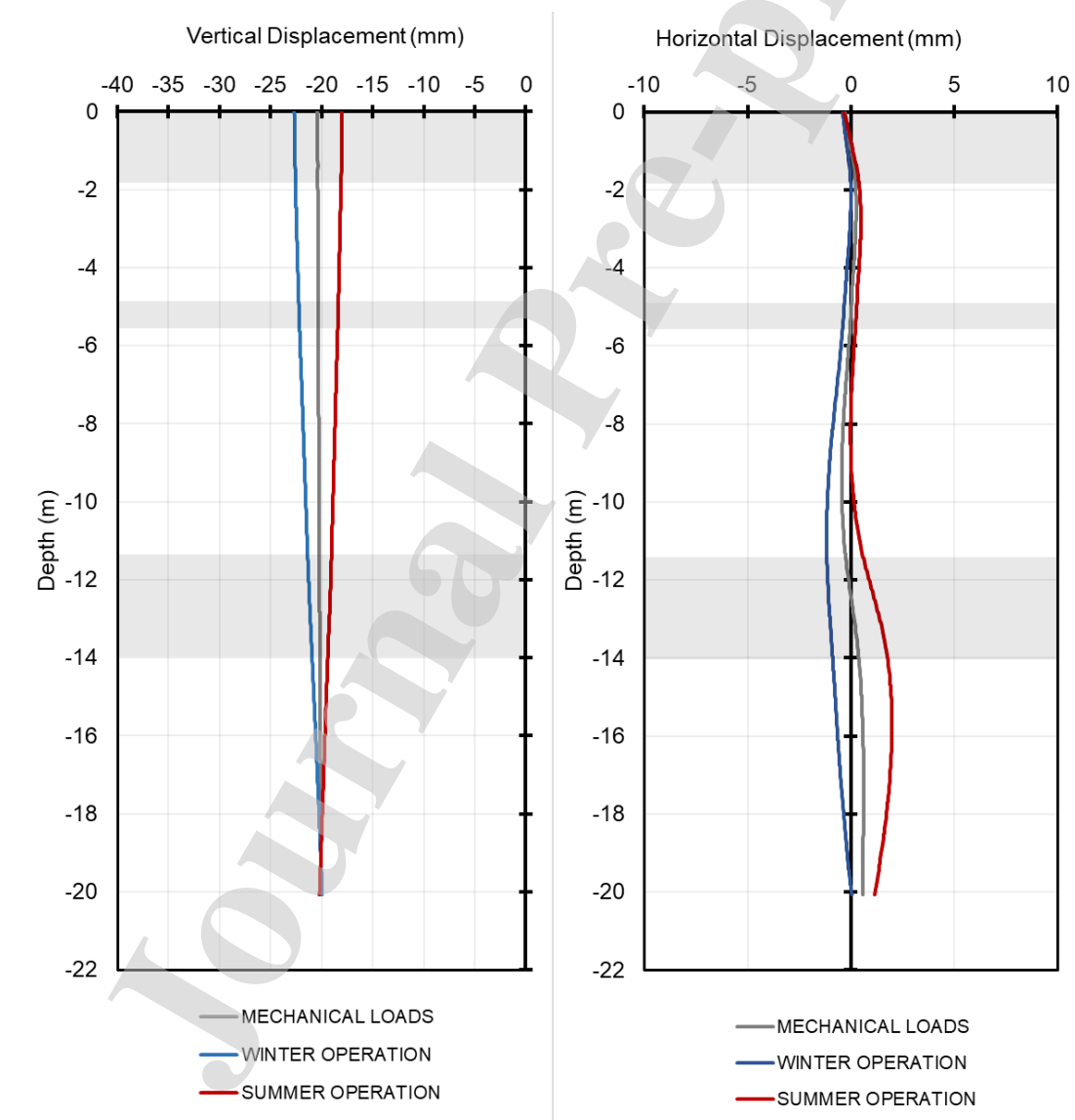
570 Figure 14 Comparison of the experimental and numerical results for the heating (December 2019) and cooling (March 2020)  
 571 tests

572 Second, a series of numerical analyses is performed, focusing on analyzing all possible ultimate (ULS)  
 573 and serviceability (SLS) limit states accounting for simultaneous thermal and mechanical actions in  
 574 accordance with the Swiss norm (SIA 197/1, 2004; SIA 261 and 261/1, 2003; SIA 262, 2003; SIA 267  
 575 and 267/1, 2003). Along with geothermal operation and following the design details of the UEI,  
 576 additional mechanical loads are included. Details are reported in Appendix B.

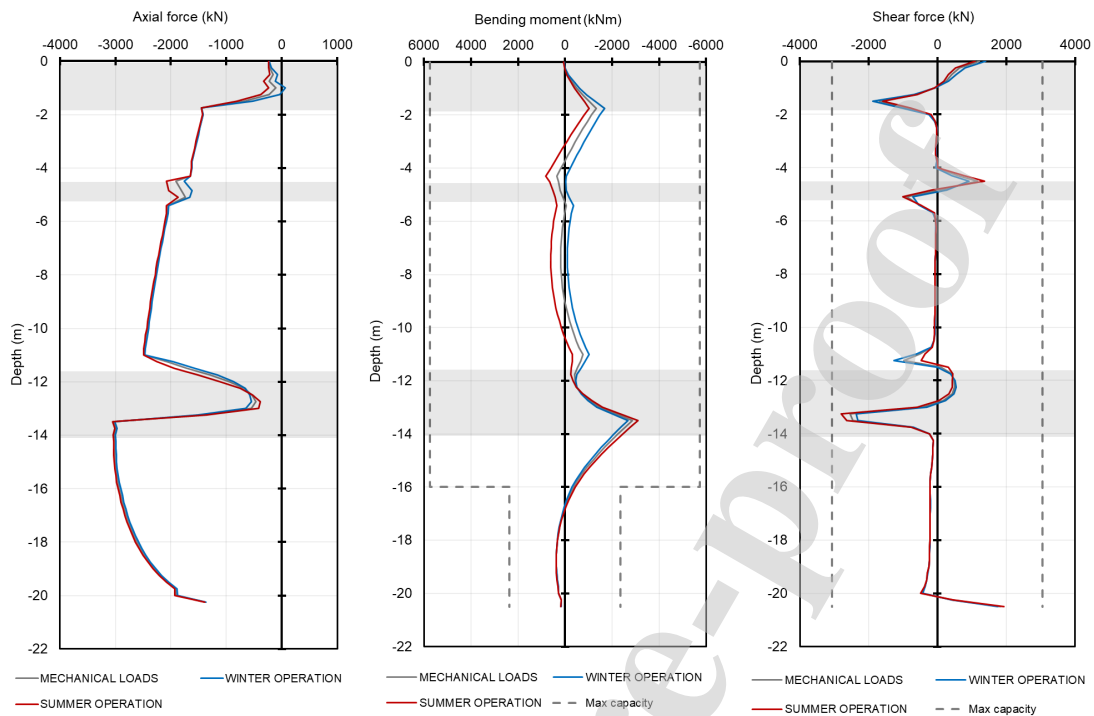
577 Figure 15 and Figure 16 show the results for the EW axial displacements and internal actions evaluated  
 578 at the cross section in correspondence with the HEs. The vertical behavior of the EW is driven by the  
 579 settlement (i.e., negative displacement) induced by applying mechanical actions. During heating, the  
 580 EW partly expands, reducing its overall settlement. The null point (Laloui and Di Donna, 2013; Rotta  
 581 Loria et al., 2020) is located at the fully embedded portion near the EW toe. The opposite was recorded  
 582 upon cooling. Thermal actions have a primary role in defining transversal (i.e., horizontal)  
 583 displacements, consequently to the bending effects induced by the nonuniform temperature distribution.

584 The recorded values largely respect the maximum acceptable limits defined by the Swiss norm (i.e., 20  
585 mm for this geometry).

586 Internal actions follow the general behavior defined by the mechanical load application, with major  
587 variations located at the wall-slab connections due to structural stress redistribution within the structure,  
588 particularly for axial force and shear force. The bending moment shows larger discrepancies **between**  
589 the isothermal and nonisothermal cases. A positive bending moment (Figure 16) upon heating means  
590 that traction develops at the intrados, while contraction develops at the extrados due to the blocked  
591 portion of thermal expansion during heating (i.e., summer operation). The opposite was recorded during  
592 cooling (i.e., winter operation). The maximum capacity of the structure (i.e., resistance bending  
593 moment, shear force, axial force) is respected.



595 Figure 15 Wall axis vertical and horizontal displacements at SLS: results from 3D numerical thermomechanical modeling



597

Figure 16 Internal actions in the wall at the ULS: results from 3D numerical thermomechanical modeling

## 598 6. Concluding remarks

599 This study presents the results from an experimental campaign on a full-scale underground energy  
 600 infrastructure (i.e., an underground railway station) and the related numerical modeling. The main  
 601 concluding remarks related to its THM behavior are summarized as follows.

602 The wall-tunnel hydrothermal interactions show a strong correlation between the tunnel temperature  
 603 and external temperature, with high seasonal temperature variations. A relatively low speed, low scatter  
 604 wind speed profile, compared with measurements on existing tunnels available in the literature (He et  
 605 al., 2020; Jin et al., 2020; Pflitsch et al., 2012; Pflitsch and Kuesel, 2003; Steinemann et al., 2004;  
 606 Woods and Pope, 1981; Zhao et al., 2020), was recorded. Low-magnitude wind speed induces low  
 607 convective heat exchanges and hence low heat flux at the wall-tunnel interface. Additionally, the  
 608 presence of a glass wall in the tunnel dramatically reduces the wind velocity profile near the EW,  
 609 highlighting the boundary layer of the wind at the wall-tunnel interface. Thus, the tunnel, under certain  
 610 circumstances, may act as a thermal resistance rather than as a conductor.

611 High seasonal temperature variations at the boundary conditions induce nonnegligible yearly  
 612 temperature variations within the UEI. This is because the UEI is located at the thermal and  
 613 hydrodynamic (Laloui & Rotta Loria, 2019; Peltier et al., 2019) entrance regions of the tunnel.

614 The UEI shows a very high heat storage potential (i.e., summer operation). The key aspects that  
 615 highlight the heat storage potential are as follows: (i) the predominant heat exchange mechanism is

616 conduction in the wall and in the soil, with absence of groundwater flow in the soil; (ii) the low heat  
 617 flux magnitude at the wall intrados minimizes heat losses toward the tunnel, which acts as a natural  
 618 insulator; and (iii) the high capacity of storing heat develops high HCF temperature differences between  
 619 the inflow and outlet during heating tests.

620 During winter operation (i.e., EW cooling), the UEI has a limited operative HCF temperature range.  
 621 The use of glycolized fluids to replace water is strongly suggested for future operations, as it would  
 622 allow HCF temperatures to be reached  $T_f < 0$  °C, avoiding freezing issues within the HP and  
 623 surroundings and consequently increasing the thermal potential.

624 From a thermomechanical perspective, the UEI is very stiff. It can hence undergo high internal actions  
 625 while mobilizing little displacement (i.e., high mechanical capacity). The design limits are successfully  
 626 respected.

627

## 628 Acknowledgments

629 The authors wish to acknowledge the financial support of SIG (Services Industriels de Genève) through  
 630 the project “Modélisation des géo-structures énergétiques de la gare CEVA CABA.”

631

## 632 References

- 633 Adam, D., Markiewicz, R., 2009. Energy from earth-coupled structures, foundations, tunnels and  
 634 sewers. *Géotechnique* 59, 229–236. <https://doi.org/10.1680/geot.2009.59.3.229>
- 635 Asadi, I., Shafiqh, P., Abu Hassan, Z.F.B., Mahyuddin, N.B., 2018. Thermal conductivity of concrete  
 636 – A review. *J. Build. Eng.* 20, 81–93. <https://doi.org/10.1016/j.job.2018.07.002>
- 637 Batini, N., Rotta Loria, A.F., Conti, P., Testi, D., Grassi, W., Laloui, L., 2015. Energy and geotechnical  
 638 behaviour of energy piles for different design solutions. *Appl. Therm. Eng.* 86, 199–213.  
 639 <https://doi.org/10.1016/j.applthermaleng.2015.04.050>
- 640 Bourne-Webb, P., Burlon, S., Javed, S., Kürten, S., Loveridge, F., 2016. Analysis and design methods  
 641 for energy geostructures. *Renew. Sustain. Energy Rev.* 65, 402–419.  
 642 <https://doi.org/10.1016/j.rser.2016.06.046>
- 643 Bourne-Webb, P.J., Bodas Freitas, T.M., da Costa Gonçalves, R.A., 2016. Thermal and mechanical  
 644 aspects of the response of embedded retaining walls used as shallow geothermal heat  
 645 exchangers. *Energy Build.* 125, 130–141. <https://doi.org/10.1016/j.enbuild.2016.04.075>
- 646 Bowles, J.E., 1988. *Foundation analysis and design*, Fourth Edition, McGraw-Hill Book Company. ed.  
 647 USA.
- 648 Brandl, H., 2016. Geothermal Geotechnics for Urban Undergrounds. *Procedia Eng.*, 15th International  
 649 scientific conference “Underground Urbanisation as a Prerequisite for Sustainable  
 650 Development” 12-15 September 2016, St. Petersburg, Russia 165, 747–764.  
 651 <https://doi.org/10.1016/j.proeng.2016.11.773>
- 652 Brandl, H., 2006. Energy foundations and other thermo-active ground structures. *Géotechnique* 56, 81–  
 653 122. <https://doi.org/10.1680/geot.2006.56.2.81>
- 654 Carslaw, H.S., Jaeger, J.C., 1952. *Conduction of Heat in Solids*. Clarendon Press.
- 655 CFMS-SYNTEC-SOFFONS-FNTP, 2017. *Recommandations pour la conception, le dimensionnement*  
 656 *et la mise en oeuvre des géostructures thermiques*, pp. 120.

- 657 COMSOL Inc., 2018. COMSOL Multiphysics Reference Manual, version 5.3. [www.comsol.com](http://www.comsol.com).
- 658 Di Donna, A., 2016. Energy walls for an underground car park. 25th Eur. Young Geotech. Eng. Conf.  
659 21–24.
- 660 Di Donna, A., Barla, M., Amis, T., 2017. Energy Geostructures: Analysis from research and systems  
661 installed around the World, in: DFI 42nd Annual Conference on Deep Foundations. New  
662 Orleans, United States.
- 663 Gao, L., Zhao, J., Tang, Z., 2015. A review on borehole seasonal solar thermal energy storage. *Energy*  
664 *Procedia* 70, 209–218.
- 665 Gehlin, S., 2016. 11 - Borehole thermal energy storage, in: Rees, S.J. (Ed.), *Advances in Ground-Source*  
666 *Heat Pump Systems*. Woodhead Publishing, pp. 295–327. <https://doi.org/10.1016/B978-0-08-100311-4.00011-X>
- 667 Gehlin, S., 2002. Thermal response test : method development and evaluation.
- 668 Gehlin, S., Hellström, G., 2000. Recent status of in-situ thermal response tests for BTES applications  
669 in Sweden. *Proc Terrastock 2000* 159–164.
- 670 Gnielinski, V., 1976. New equations for heat and mass transfer in turbulent pipe and channel flow. *Int*  
671 *Chem Eng* 16, 359–368.
- 672 GSHPA, G.S.H.P.A., 2012. Thermal piles standard.
- 673 Guo, Lixia, Guo, Lei, Zhong, L., Zhu, Y., 2011. Thermal conductivity and heat transfer coefficient of  
674 concrete. *J. Wuhan Univ. Technol.-Mater Sci Ed* 26, 791–796. [https://doi.org/10.1007/s11595-](https://doi.org/10.1007/s11595-011-0312-3)  
675 [011-0312-3](https://doi.org/10.1007/s11595-011-0312-3)
- 676 Haaland, S.E., 1983. Simple and Explicit Formulas for the Friction Factor in Turbulent Pipe Flow. *J.*  
677 *Fluids Eng.* 105, 89–90. <https://doi.org/10.1115/1.3240948>
- 678 He, X., Li, A., Ning, Y., 2020. Optimization of outdoor design temperature for summer ventilation for  
679 undersea road tunnel using field measurement and statistics. *Build. Environ.* 167, 106457.  
680 <https://doi.org/10.1016/j.buildenv.2019.106457>
- 681 Jin, S., Jin, J., Gong, Y., 2020. A theoretical explanation of natural ventilation at roof openings in urban  
682 road tunnels. *Tunn. Undergr. Space Technol.* 98, 103345.  
683 <https://doi.org/10.1016/j.tust.2020.103345>
- 684 Kavanaugh, S.P., Rafferty, K.D., 2014. *Geothermal heating and cooling: design of ground-source heat*  
685 *pump systems*, ASHRAE. ed. ASHRAE, Atlanta.
- 686 Laloui, L., Di Donna, A., 2013. *Energy geostructures: Innovation in Underground Engineering*, ISTE  
687 and John Wiley&Sons. ed. Hoboken, NJ, USA.
- 688 Laloui, L., Nuth, M., Vulliet, L., 2006. Experimental and numerical investigations of the behaviour of  
689 a heat exchanger pile. *Int. J. Numer. Anal. Methods Geomech.* 30, 763–781.  
690 <https://doi.org/10.1002/nag.499>
- 691 Laloui, L., Rotta Loria, A.F., 2019. *Analysis and Design of Energy Geostructures - 1st Edition*.  
692 Academic Press.
- 693 Lambe, T.W., Whitman, R.V., 1991. *Soil Mechanics*. John Wiley & Sons.
- 694 Lee, Y., Choi, M.-S., Yi, S.-T., Kim, J.-K., 2009. Experimental study on the convective heat transfer  
695 coefficient of early-age concrete. *Cem. Concr. Compos.* 31, 60–71.  
696 <https://doi.org/10.1016/j.cemconcomp.2008.09.009>
- 697 Loria, A.F.R., Zannin, J., Llabjani, Q., Laloui, L., 2020. Analytical solution for describing the thermo-  
698 mechanical behavior of plane energy geostructures. *E3S Web Conf.* 205, 06009.  
699 <https://doi.org/10.1051/e3sconf/202020506009>
- 700 Loveridge, F. a., Olgun, C. g., Brettmann, T., Powrie, W., 2015. Group thermal response testing for  
701 energy piles, in: *Geotechnical Engineering for Infrastructure and Development, Conference*  
702 *Proceedings*. ICE Publishing, pp. 2595–2600. <https://doi.org/10.1680/ecsmge.60678.vol5.400>
- 703 Loveridge, F., McCartney, J.S., Narsilio, G.A., Sanchez, M., 2020. Energy geostructures: A review of  
704 analysis approaches, in situ testing and model scale experiments. *Geomech. Energy Environ.*  
705 22, 100173. <https://doi.org/10.1016/j.gete.2019.100173>
- 706 Makasis, N., Narsilio, G.A., 2020. Energy diaphragm wall thermal design: The effects of pipe  
707 configuration and spacing. *Renew. Energy* 154, 476–487.  
708 <https://doi.org/10.1016/j.renene.2020.02.112>
- 709



- 710 Makasis, N., Narsilio, G.A., Bidarmaghz, A., Johnston, I.W., Zhong, Y., 2020. The importance of  
711 boundary conditions on the modelling of energy retaining walls. *Comput. Geotech.* 120,  
712 103399. <https://doi.org/10.1016/j.compgeo.2019.103399>
- 713 Mattsson, N., Steinmann, G., Laloui, L., 2008. Advanced compact device for the in situ determination  
714 of geothermal characteristics of soils. *Energy Build.* 40, 1344–1352.  
715 <https://doi.org/10.1016/j.enbuild.2007.12.003>
- 716 Mimouni, T., Laloui, L., 2015. Behaviour of a group of energy piles. *Can. Geotech. J.* 52, 1913–1929.  
717 <https://doi.org/10.1139/cgj-2014-0403>
- 718 Nicholson, D.P., Chen, Q., de Silva, M., Winter, A., Winterling, R., 2014. The design of thermal tunnel  
719 energy segments for Crossrail, UK. *Proc. Inst. Civ. Eng. - Eng. Sustain.* 167, 118–134.  
720 <https://doi.org/10.1680/ensu.13.00014>
- 721 Nordell, B., Andersson, O., Rydell, L., Scorpo, A.L., 2015. Long-term Performance of the HT-BTES  
722 in Emmaboda, Sweden. Presented at the Greenstock 2015 : International Conference on  
723 Underground Thermal Energy Storage 19/05/2015 - 21/05/2015.
- 724 Pahud, D., Matthey, B., 2001. Comparison of the thermal performance of double U-pipe borehole heat  
725 exchangers measured in situ. *Energy Build.*, Special Issue: Proceedings of the International  
726 Conference on 33, 503–507. [https://doi.org/10.1016/S0378-7788\(00\)00106-7](https://doi.org/10.1016/S0378-7788(00)00106-7)
- 727 Peltier, M., Rotta Loria, A.F., Lepage, L., Garin, E., Laloui, L., 2019. Numerical investigation of the  
728 convection heat transfer driven by airflows in underground tunnels. *Appl. Therm. Eng.* 159,  
729 113844. <https://doi.org/10.1016/j.applthermaleng.2019.113844>
- 730 Pflitsch, A., Bruene, M., Steiling, B., Killing-Heinze, M., Agnew, B., Irving, M., Lockhart, J., 2012.  
731 Air flow measurements in the underground section of a UK light rail system. *Appl. Therm.*  
732 *Eng.* 32, 22–30. <https://doi.org/10.1016/j.applthermaleng.2011.07.030>
- 733 Pflitsch, A., Kuesel, H., 2003. Subway-Climatology–New research Field for the Management of  
734 possible Catastrophes in subway systems. *Man Clim. 20th Century Stud. Geogr.* 75, 384–394.
- 735 Reuss, M., 2015. 6 - The use of borehole thermal energy storage (BTES) systems, in: Cabeza, L.F.  
736 (Ed.), *Advances in Thermal Energy Storage Systems*, Woodhead Publishing Series in Energy.  
737 Woodhead Publishing, pp. 117–147. <https://doi.org/10.1533/9781782420965.1.117>
- 738 Rotta Loria, A.F., Bocco, M., Garbellini, C., Muttoni, A., Laloui, L., 2020. The role of thermal loads in  
739 the performance-based design of energy piles. *Geomech. Energy Environ.* 21, 100153.  
740 <https://doi.org/10.1016/j.gete.2019.100153>
- 741 Rotta Loria, A.F., Laloui, L., 2017a. Thermally induced group effects among energy piles.  
742 *Géotechnique* 67, 374–393. <https://doi.org/10.1680/jgeot.16.P.039>
- 743 Rotta Loria, A.F., Laloui, L., 2017b. Group action effects caused by various operating energy piles.  
744 *Géotechnique* 68, 834–841. <https://doi.org/10.1680/jgeot.17.P.213>
- 745 Sanner, B., Hellström, G., Spitler, J., Gehlin, S., 2005. Thermal response test—current status and world-  
746 wide application, in: *Proceedings World Geothermal Congress. International Geothermal*  
747 *Association*, pp. 24–29.
- 748 Shafagh, I., Rees, S., Urta Mardaras, I., Curto Janó, M., Polo Carbayo, M., 2020. A Model of a  
749 Diaphragm Wall Ground Heat Exchanger. *Energies* 13, 300.  
750 <https://doi.org/10.3390/en13020300>
- 751 SIA 197/1, 2004. *Projets de tunnels, tunnels ferroviaires*. Société suisse des ingénieurs et des  
752 architectes, Zurich.
- 753 SIA 261 and 261/1, 2003. “Actions sur les structures porteuses” et “Actions sur les structures porteuses  
754 – spécifications complémentaires”. Société suisse des ingénieurs et des architectes, Zurich.
- 755 SIA 262, 2003. *Construction en béton*. Société suisse des ingénieurs et des architectes, Zurich.
- 756 SIA 267 and 267/1, 2003. “Géotechnique” et “Géotechnique –spécifications complémentaires”. Société  
757 suisse des ingénieurs et des architectes, Zurich.
- 758 SIA D0190, 2005. *Utilisation de la Chaleur du Sol par des Ouvrages de Fondation et de Soutènement*  
759 *en Béton. Guide pour la Conception, la Realisation et la Maintenance*.
- 760 Steinemann, U., Zumsteg, F., Wildi, P., 2004. Measurements of air flow, temperature differences and  
761 pressure differences in road tunnels. *Int. Conf. Tunn. Saf. Vent. Graz Austria* 220–226.
- 762 Sterpi, D., Angelotti, A., Habibzadeh-Bigdarvish, O., Jalili, D., 2018. Assessment of thermal behaviour  
763 of thermo-active diaphragm walls based on monitoring data. *J. Rock Mech. Geotech. Eng.* 10,  
764 1145–1153. <https://doi.org/10.1016/j.jrmge.2018.08.002>

- 765 Sterpi, D., Tomaselli, G., Angelotti, A., 2020. Energy performance of ground heat exchangers  
766 embedded in diaphragm walls: Field observations and optimization by numerical modelling.  
767 *Renew. Energy, Shallow Geothermal Energy Systems* 147, 2748–2760.  
768 <https://doi.org/10.1016/j.renene.2018.11.102>
- 769 Sutman, M., Speranza, G., Ferrari, A., Larrey-Lassalle, P., Laloui, L., 2020. Long-term performance  
770 and life cycle assessment of energy piles in three different climatic conditions. *Renew. Energy*  
771 146, 1177–1191. <https://doi.org/10.1016/j.renene.2019.07.035>
- 772 Truesdell, C., 1960. *The rational mechanics of flexible or elastic bodies 1638–1788. Leonhardi Euleri*  
773 *Opera Omnia, Turici : Venditioni exponunt Orell Füssli(IS). ed. 2. Zürich.*
- 774 Valore, R., 1980. Calculations of U-values of hollow concrete masonry. *Concr. Int.* 2, 40–63.
- 775 Vulliet, L., Laloui, L., Zhao, J., 2016. *Mécanique des sols et des roches (TGC volume 18): avec*  
776 *écoulements souterrains et transferts de chaleur. PPUR Presses polytechniques.*
- 777 Witte, H.J.L., Van Gelder, A.J., 2007. Three years monitoring of a borehole thermal energy store of a  
778 UK office building, in: Paksoy, H.Ö. (Ed.), *Thermal Energy Storage for Sustainable Energy*  
779 *Consumption, NATO Science Series. Springer Netherlands, Dordrecht, pp. 205–219.*  
780 [https://doi.org/10.1007/978-1-4020-5290-3\\_11](https://doi.org/10.1007/978-1-4020-5290-3_11)
- 781 Woods, W.A., Pope, C.W., 1981. A generalised flow prediction method for the unsteady flow generated  
782 by a train in a single-track tunnel. *J. Wind Eng. Ind. Aerodyn.* 7, 331–360.  
783 [https://doi.org/10.1016/0167-6105\(81\)90057-X](https://doi.org/10.1016/0167-6105(81)90057-X)
- 784 Xia, C., Sun, M., Zhang, G., Xiao, S., Zou, Y., 2012. Experimental study on geothermal heat exchangers  
785 buried in diaphragm walls. *Energy Build.* 52, 50–55.  
786 <https://doi.org/10.1016/j.enbuild.2012.03.054>
- 787 Zannin, J., 2020. Thermomechanical behavior of underground energy infrastructures. Ph.D. thesis nr.  
788 8450, Swiss Federal Institute of Technology in Lausanne, EPFL.
- 789 Zannin, J., Ferrari, A., Larrey-Lassalle, P., Laloui, L., 2020a. Early-stage thermal performance design  
790 of thermo-active walls implemented in underground energy infrastructures. *Geomech. Energy*  
791 *Environ.*
- 792 Zannin, J., Ferrari, A., Pousse, M., Laloui, L., 2020b. Hydrothermal interactions in energy walls.  
793 *Undergr. Space.* <https://doi.org/10.1016/j.undsp.2020.02.001>
- 794 Zannin, J., Ferrari, A., Pousse, M., Laloui, L., 2019. Thermal design and full-scale thermal response  
795 test on Energy Walls. *E3S Web Conf.* 92, 18011. <https://doi.org/10.1051/e3sconf/20199218011>
- 796 Zannin, J., Rotta Loria, A.F., Llabjani, Q., Laloui, L., 2020c. Extension of Winkler’s solution to non-  
797 isothermal conditions for capturing the behaviour of plane geostructures subjected to thermal  
798 and mechanical actions. *Comput. Geotech.*
- 799 Zhang, W., Min, H., Gu, X., Xi, Y., Xing, Y., 2015. Mesoscale model for thermal conductivity of  
800 concrete. *Constr. Build. Mater.* 98, 8–16. <https://doi.org/10.1016/j.conbuildmat.2015.08.106>
- 801 Zhao, P., Chen, J., Luo, Y., Li, Y., Chen, L., Wang, C., Hu, T.T., 2020. Field measurement of air  
802 temperature in a cold region tunnel in northeast China. *Cold Reg. Sci. Technol.* 171, 102957.  
803 <https://doi.org/10.1016/j.coldregions.2019.102957>
- 804

805

806 **Appendix A: Details of the numerical model**

807 The mathematical formulation for the finite element models used in this study is reported here. The  
 808 thermo-hydro-mechanical behavior is described by the following equations. Concrete and soil are  
 809 modeled as fully saturated porous materials with no groundwater flow.

810 The mass conservation equation of the fluid phase in the porous media reads:

$$\frac{\partial}{\partial t}(n \rho_w) + \text{div}(\rho_w \mathbf{v}_{rw}) = 0 \quad (\text{A.1})$$

811 where  $n$  is the porosity of the porous medium,  $\rho_w$  is the fluid density,  $t$  is the time, and  $\mathbf{v}_{rw} = \mathbf{0}$  is the  
 812 fluid velocity according to Darcy's law.

813 The energy conservation equation can be separated into two parts: one that relates to the conductive and  
 814 convective heat transfer processes in the porous materials and another to the hydrothermal fluid flow  
 815 inside the heat exchangers.

816 The former part can be written as

$$\text{div}(\lambda \mathbf{grad}T) = \rho C_p \frac{\partial T}{\partial t} + \rho_w C_{p,w} \mathbf{v}_{rw} \cdot \mathbf{grad}T \quad (\text{A.2})$$

817 in which  $\lambda$  is the thermal conductivity of the effective material:

$$\lambda = (1 - n)\lambda_s + n\lambda_w \quad (\text{A.3})$$

818 where the subscripts  $s$  and  $w$  relate to the solid and fluid phases, respectively.  $T$  is the temperature, and  
 819  $\rho C_p$  is the effective volumetric heat capacity at constant pressure:

$$\rho C_p = (1 - n)\rho_s C_{p,s} + n\rho_w C_{p,w} \quad (\text{A.4})$$

820 The second part of the energy conservation equation relating to the nonisothermal fluid flow inside the  
 821 heat exchangers accounts for the convective heat exchanges within the fluid and for conduction through  
 822 the pipe wall:

$$\rho_f c_f A_p \frac{\partial T_{bulk,f}}{\partial t} + \rho_f c_f A_p \mathbf{u}_f \cdot \mathbf{grad}(T_{bulk,f}) = \text{div}[A_p \lambda_f \mathbf{grad}(T_{bulk,f})] + \dot{q}_p \quad (\text{A.5})$$

823 where  $\rho_f$ ,  $c_f$ ,  $T_{bulk,f}$ ,  $\mathbf{u}_f$ ,  $\lambda_f$  are the bulk density, specific heat at constant pressure, bulk temperature,  
 824 tangential velocity and thermal conductivity of the fluid, respectively. The cross section of the heat  
 825 exchanger pipe is  $A_p$ , and  $\dot{q}_p$  expresses the heat flux per unit length through the pipe wall, which is  
 826 defined as:

$$\dot{q}_p = UP_p(T_{ext} - T_{bulk,f}) \quad (\text{A.6})$$

827 where  $U$  relates to an effective value of the pipe heat transfer coefficient accounting for the thermal  
 828 resistances of the internal film and the wall.  $U$  is expressed as a function of the hydraulic radius, pipe  
 829 geometry and thermal conductivity of the pipe material.  $P_p = 2\pi r_{int}$  is the wetted perimeter of the pipe  
 830 cross section, and  $T_{ext}$  is the external temperature of the pipe (Batini et al., 2015; COMSOL Inc., 2018;  
 831 Gnielinski, 1976; Haaland, 1983; Zannin et al., 2020b).

832 The equilibrium equation reads as:

$$\text{div } \boldsymbol{\sigma} + \rho \mathbf{g} = 0 \quad (\text{A.7})$$

833 where  $\text{div}$  denotes the divergence operator,  $\boldsymbol{\sigma}$  is the total stress tensor,  $\rho$  is the density of the porous  
 834 material, and  $\mathbf{g}$  is the gravity vector. In the framework of thermo-elasticity, when drained conditions  
 835 are considered (*i.e.*, variations in total stress are equivalent to variations in effective stress), the  
 836 constitutive law reads:

$$d\boldsymbol{\sigma} = \mathbf{C}(d\boldsymbol{\varepsilon} + \boldsymbol{\beta}dT) \quad (\text{A.8})$$

837 where  $\mathbf{C}$  is the constitutive tensor,  $\boldsymbol{\varepsilon}$  is the total strain tensor,  $\boldsymbol{\beta}$  is a tensor that contains the thermal  
 838 expansion coefficient ( $\alpha$ ) in the main diagonal, and  $T$  is the temperature.

839 With reference to the model geometry presented in Figure 8, the external mechanical loads detailed in  
 840 Appendix B are applied as surface loads. The results from piezometric readings (dated to 2008) at a  
 841 location approximately 150 m from the considered cross section (*i.e.*, Figure 1) suggest that the  
 842 groundwater table is located in the gravel layer. The following hydraulic boundaries are set: for SLS  
 843 calculations, the groundwater table is considered at the top of layer D (Figure 1, Table 1) and under  
 844 hydrostatic conditions; hence, negative pore water pressures develop above the groundwater table, and  
 845 the materials are considered saturated (saturated unit weight,  $\gamma_{sat}$ ); for ULS calculations, an additional  
 846 case is defined, aiming at defining a worst-case scenario, which foresees the groundwater table located  
 847 at the top of layer B (*i.e.*, at the top of the geostructure) and under hydrostatic conditions. Under these  
 848 conditions, layers B, C and D are below the groundwater table (*i.e.*, characterized by their submerged  
 849 unit weight,  $\gamma'$ ). These two conditions are used in the definition of the combinations of actions together  
 850 with the thermal and mechanical loads reported in Appendix B.

851 First, the model is hydromechanically initialized at rest ( $K_0$ ) conditions and at a uniform temperature  
 852  $T_s = 14.5$  °C. This assumption is a simplification of reality. No details and monitoring during the  
 853 construction processes are available, making completely arbitrary, at this stage, any attempt to consider  
 854 thermomechanical aspects during the construction process, which occurred more than 5 years before  
 855 the execution of the first thermal tests (*i.e.*, the TRT in August 2019). Additionally, the geostructural  
 856 response following the hypothesis of elasticity of all materials (Figure 14) seems to give a satisfactory  
 857 representation of reality.

858 Second, a transient analysis is performed. In addition to the hydromechanical description reported at  
 859 the first step, thermal boundary conditions (reported in section 4.1) are simulated for 10 years to ensure  
 860 a periodical response independent of the initial conditions.

861 Third, thermomechanical loads are applied. They involve the concurrent application of the thermal input  
 862 induced by geothermal operation for winter and summer, together with the combinations of mechanical  
 863 loads taken following the Swiss norms (Appendix B).

864

#### 865 **Appendix B: Rationale for applying mechanical loads**

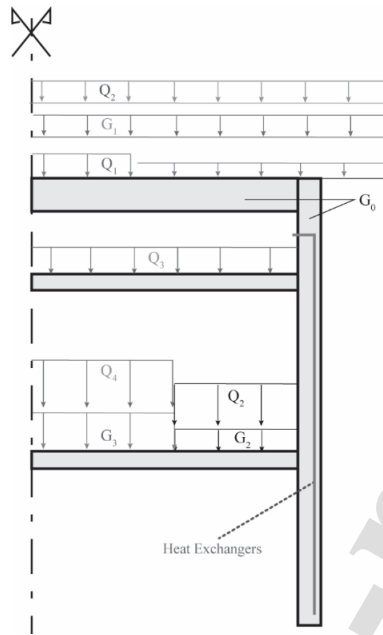
866 This appendix expands on the additional thermomechanical loads accounted for during the analyses  
 867 reported in section 5. In conjunction with thermal operation, the following mechanical loads are  
 868 considered: train load, ballast load and structural surcharges at level -2, crowding load at level -1, road  
 869 traffic, embankment and pedestrian surcharges at level 0 (Figure 17 and Table D.1). Following the  
 870 Swiss norm, the following load combinations for the ULS (equation D.1) and SLS (equation D.2) are  
 871 considered:

$$1.35 \sum_i G_i + 1.5 \left( \sum_i Q_i + q_T T \right) \quad (\text{D.1})$$

$$\sum_i G_i + \sum_i Q_i + q_T T \quad (\text{D.2})$$

$$\sum_i G_i + 0.6 \sum_i Q_i + T$$

872 where  $G_i$  and  $Q_i$  are detailed in Table B.1, and  $T$  represents the yearly profile of heat carrier fluid  
 873 temperature imposed at the inflow point (i.e., 6 months of heating followed by 6 months of cooling).  
 874  $q_T = 0.6$  represents a nondimensional multiplier from the Swiss norm.



876 Figure 17 Sketch of the geostructural geometry over a vertical cross section corresponding to the heat exchangers with  
 877 indications of the mechanical loads detailed in

878 Table B.1 Description of the mechanical loads considered for the thermomechanical analysis

Name	Description	Characteristic value	Unit
<i>Dead loads</i>			
$G_0$	Structure unit weight	25.0	kN/m <sup>3</sup>
$G_1$	Embankment surcharge	56.0	kN/m <sup>2</sup>
$G_2$	Structural surcharge	40.0	kN/m <sup>2</sup>
$G_3$	Rail ballast	22.0	kN/m <sup>2</sup>
<i>Live loads</i>			
$Q_1$	Road traffic (tramway)	26.6	kN/m <sup>2</sup>
		2.3	kN/m <sup>2</sup>
$Q_2$	Pedestrian load	4.0	kN/m <sup>2</sup>
$Q_3$	Crowding surcharge	10.0	kN/m <sup>2</sup>
$Q_4$	Train load	92.4	kN/m <sup>2</sup>

879

880

- Full-scale in-situ investigations on underground energy infrastructures involves coupled THM aspects
- Hydrothermal infrastructure monitoring allows to understand how it affects geothermal operations
- Heat storage and extraction potential is affected also by the hydrothermal conditions at air interfaces
- Guidelines on thermal response test execution for underground infrastructures are proposed
- Thermomechanical behavior of the retaining walls involve thermally-induced axial and flexural actions

**Jacopo Zannin:** Conceptualization, Methodology, Validation, Formal analysis, Investigation, Resources, Data Curation, Writing – Original draft, Writing – review and editing, Visualization, Project administration

**Alessio Ferrari:** Conceptualization, Validation, Resources, Writing – Original draft, Writing – review and editing, Supervision, Project administration

**Tohid Kazerani:** Validation, Investigation, Resources, Project administration

**Azad Koliji:** Validation, Resources, Writing – review and editing, Supervision, Project administration, Funding acquisition

**Lyesse Laloui:** Validation, Resources, Writing – review and editing, Supervision, Project administration, Funding acquisition



**Declaration of interests**

The authors declare that they have no known competing financial interests or personal relationships that could have appeared to influence the work reported in this paper.

The authors declare the following financial interests/personal relationships which may be considered as potential competing interests:

Journal Pre-proof